

# ***Chandra* studies of the globular cluster 47 Tucanae: a deeper X-ray source catalogue, five new X-ray counterparts to millisecond radio pulsars and new constraints to r-mode instability window**

Souradeep Bhattacharya,<sup>1,2★</sup> Craig O. Heinke,<sup>2</sup> Andrey I. Chugunov,<sup>3</sup>  
Paulo C. C. Freire,<sup>4</sup> Alessandro Ridolfi<sup>4</sup> and Slavko Bogdanov<sup>5</sup>

<sup>1</sup>*Birla Institute of Technology and Science, Pilani 333031, India*

<sup>2</sup>*Physics Department, University of Alberta, 4-183 CCIS, Edmonton, AB T6G 2G7, Canada*

<sup>3</sup>*Ioffe Institute, Polytekhnicheskaya 26, 194021 St. Petersburg, Russia*

<sup>4</sup>*Max-Planck-Institut für Radioastronomie, Auf dem Hügel 69, D-53121 Bonn, Germany*

<sup>5</sup>*Columbia Astrophysics Laboratory, Columbia University, 550 West 120th Street, New York, NY 10027, USA*

Accepted 2017 August 28. Received 2017 August 4; in original form 2017 January 5

## **ABSTRACT**

We combined *Chandra* ACIS observations of the globular cluster 47 Tucanae (47 Tuc) from 2000, 2002 and 2014–2015 to create a deeper X-ray source list, and study some of the faint radio millisecond pulsars (MSPs) present in this cluster. We have detected 370 X-ray sources within the half-mass radius (2.79 arcsec) of the cluster, 81 of which are newly identified, by including new data and using improved source detection techniques. The majority of the newly identified sources are in the crowded core region, indicating cluster membership. We associate five of the new X-ray sources with chromospherically active BY Dra or W UMa variables identified by Albrow et al. We present alternative positions derived from two methods, centroiding and image reconstruction, for faint, crowded sources. We are able to extract X-ray spectra of the recently discovered MSPs 47 Tuc aa, 47 Tuc ab, the newly timed MSP 47 Tuc Z, and the newly resolved MSPs 47 Tuc S and 47 Tuc F. Generally, they are well fitted by blackbody or neutron star atmosphere models, with temperatures, luminosities and emitting radii similar to those of other known MSPs in 47 Tuc, though 47 Tuc aa and 47 Tuc ab reach lower X-ray luminosities. We limit X-ray emission from the full surface of the rapidly spinning (542 Hz) MSP 47 Tuc aa, and use this limit to put an upper bound for amplitude of r-mode oscillations in this pulsar as  $\alpha < 2.5 \times 10^{-9}$  and constrain the shape of the r-mode instability window.

**Key words:** stars: neutron – pulsars: general – globular clusters: individual: NGC 104.

## **1 INTRODUCTION**

In the cores of globular clusters (GCs), the very high stellar densities result in an extremely high rate of dynamical interactions. These produce a large number and variety of close binary systems, many of them unique to this environment, including low-mass X-ray binaries (LMXBs; Clark 1975), radio millisecond pulsars (MSPs; Johnston, Kulkarni & Phinney 1992), X-ray active binaries (ABs; Bailyn, Grindlay & Garcia 1990; Dempsey et al. 1993; Grindlay et al. 2001a) and cataclysmic variables (CVs; Pooley et al. 2003), which can engage in mass transfer. Such compact binaries in GCs have been effectively discovered by recent X-ray studies, especially using the *Chandra X-Ray Observatory* (reviews include Verbunt & Lewin 2004, and Heinke 2010). Detailed analyses of such sources

have also made it possible to probe deeper into the formation and evolution of such remarkable objects (Ivanova et al. 2006, 2008).

MSPs are thought to have been produced from LMXBs when a low-mass companion star spins up the neutron star (NS) to millisecond periods by transferring angular momentum (Bhattacharya & van den Heuvel 1991; Papitto et al. 2013). MSPs can produce X-ray radiation of both thermal origin – blackbody-like radiation from a portion of the NS surface around the magnetic poles, heated by a flow of relativistic particles in the pulsar magnetosphere (Harding & Muslimov 2002) – and non-thermal origin, generally highly beamed and sharply pulsed emission attributed to the pulsar magnetosphere, typically described by a power law with a photon index  $\sim 1.1$ – $1.2$  (Becker & Trumper 1999; Zavlin 2007), or non-pulsed emission from a shock between the pulsar wind and a flow of matter from a non-degenerate companion, as seen in ‘redback’ or ‘black widow’ MSPs (Stappers et al. 2003; Bogdanov, Grindlay & van den Berg 2005; Gentile et al. 2014; Roberts et al. 2015). Hydrogen

\* E-mail: f2012553@pilani.bits-pilani.ac.in

atmosphere models have been quite competent at describing X-ray spectra and rotation-induced pulsations of the nearby MSPs that exhibit thermal radiation (Zavlin & Pavlov 1998; Bogdanov, Rybicki & Grindlay 2007; Bogdanov & Grindlay 2009). The high density of MSPs in GCs, and their well-known distances and reddening make them ideal targets to study the relation of thermal radiation from MSPs to other pulsar parameters (Kargaltsev et al. 2012). Additionally, a more complete study of MSPs is possible from X-ray observations, as compared to other wavelengths, because X-rays from surface hot spots of these highly compact MSPs will be bent by gravity to allow observers to see  $\sim 75$  per cent of the NS surface (Pechenick et al. 1983; Beloborodov 2002; Bogdanov et al. 2006), so that a significant number of MSPs whose radio beams do not intercept the Earth should still be detectable in X-rays.

X-ray studies of MSPs also allow interesting constraints on the thermal physics of their cores. In addition to external return current heating, MSPs can be heated up by internal heating mechanisms, namely, superfluid vortex creep (Alpar et al. 1984), rotochemical heating (Reisenegger 1995), rotation-induced deep crustal heating (Gusakov, Kantor & Reisenegger 2015), and heating produced by the dissipation of unstable oscillation modes (e.g.  $r$  modes, Andersson et al. 2002; Reisenegger & Bonačić 2003b; Chugunov, Gusakov & Kantor 2017; Schwenzer et al. 2017). Assuming that an MSP is in thermal balance (which is reasonable, because the thermal evolution time-scale is much shorter than the spin-down time-scale for MSPs), the total power of heating should be compensated by cooling, which depends on the MSP temperature. Thus estimates of MSP temperatures (even the upper limits) can be used to constrain heating processes (see, e.g. Chugunov, Gusakov & Kantor 2017; Mahmoodifar & Strohmayer 2017; Schwenzer et al. 2017).

47 Tuc is a massive ( $M \sim 10^6 M_\odot$ , Pryor & Meylan 1993) GC with a relatively high stellar concentration, although it is not core-collapsed (Harris 1996). It is considered to possess a significant population of binaries whose properties have been altered by close encounters with other stars or binaries, by virtue of being one of the clusters with the highest predicted close encounter frequencies (Verbunt & Hut 1987; Pooley et al. 2003). We use a cluster absorbing column of  $3.5 \times 10^{20} \text{ cm}^{-2}$  (Harris 1996, 2010 revision), a distance of 4.53 kpc (Bogdanov et al. 2016; Hansen et al. 2013) and metal abundances compiled in Heinke et al. (2006). Measuring the various binary populations of clusters like 47 Tuc is crucial for understanding and modelling the dynamical encounters between binaries that produce X-ray sources in GCs (e.g. Verbunt & Meylan 1988). Observations with the ACIS instrument onboard the *Chandra* X-Ray Observatory in 2000 and 2002 have resulted in the identification of 300 X-ray sources within the half-mass radius of 47 Tuc (Grindlay et al. 2001a; Heinke et al. 2005, hereafter H05). 47 Tuc is also a subject of intense scrutiny due to the large number of MSPs residing within the cluster. There have been 25 MSPs discovered so far using the 64-m Parkes Radio Telescope (Manchester et al. 1990, 1991; Robinson et al. 1995; Camilo et al. 2000; Pan et al. 2016; Freire et al. 2017), with radio timing positions known for 23 of them (Freire et al. 2001b, 2003; Pan et al. 2016; Ridolfi et al. 2016; Freire et al. 2017, Freire & Ridolfi 2017, in preparation).

Identification of optical counterparts to X-ray sources in 47 Tuc has relied on the exquisite angular resolution of the *Hubble Space Telescope* (*HST*). Three X-ray sources with *ROSAT* positions were identified with *HST* counterparts (Paresce, de Marchi & Ferraro 1992; Paresce & de Marchi 1994; Shara et al. 1996), but large numbers of identifications became possible with the subarc-second angular resolution of *Chandra*. The deep *HST* program GO-

8267, searching for photometric variability (Gilliland et al. 2000), enabled Albrow et al. (2001, hereafter A01) to assemble a large catalogue of binaries exhibiting variability, largely dominated by BY Dra variables, with admixtures of short-period eclipsing variables, W UMa contact binaries, ‘red stragglers’ and other variables. BY Dra variables are pairs of main-sequence stars that have enhanced chromospheric variability compared to other stars of the same age, due to their more rapid rotation, produced by tidal locking; these stars also tend to be X-ray sources (e.g. Dempsey et al. 1997). The combination of *Chandra* positions and *HST* data have enabled the detection of scores of optical/ultraviolet counterparts to X-ray sources, including 42 CVs (Grindlay et al. 2001a; Edmonds et al. 2003a,b; Rivera-Sandoval et al. 2017), 61 chromospherically active binaries (Grindlay et al. 2001a; Edmonds et al. 2003a,b; H05; Knigge et al. 2006), 6 companions to radio millisecond pulsars (Edmonds et al. 2001, 2002a, 2003a; Rivera Sandoval et al. 2015; Cadelano et al. 2015), a quiescent NS low-mass X-ray binary (Edmonds et al. 2002b) and a candidate black hole binary (Bahramian et al. 2017).

Identifications of optical counterparts to X-ray sources typically rely on variability and/or unusual colours. CVs are generally bluer than the main sequence (especially in the ultraviolet), with strong  $H\alpha$  emission and variability; two of these three properties suffices to clearly identify a counterpart. Chromospherically active binaries lie up to 0.75 mag above the main sequence (due to combining light from two stars), and generally show weak  $H\alpha$  emission and variability. Millisecond pulsars and quiescent LMXBs show faint blue, variable counterparts, sometimes with  $H\alpha$  emission, and typically require extra information from X-ray spectra or detection of radio pulsations to distinguish from CVs. These methods have been used to identify numerous optical/ultraviolet counterparts in 47 Tuc (references above) and in numerous other clusters (e.g. Grindlay et al. 2001a; Pooley et al. 2002b; Kong et al. 2006; Bassa et al. 2008; Cohn et al. 2010; Lu et al. 2011; Cool et al. 2013).

We combined the 2014–2015 *Chandra* ACIS observations (Bogdanov et al. 2016) with those made in 2000 and 2002, to obtain a deeper image of 47 Tuc with improved angular resolution. In this paper, we describe the X-ray analysis we used to create a larger source catalogue with accurate source positions, and focus on the X-ray properties of the MSPs 47 Tuc F, S, Z, aa and ab, whose X-ray counterparts we have identified in this work. We have also identified new X-ray counterparts to five chromospherically active binaries previously identified by A01. We have left searches of our X-ray error circles for additional optical/UV counterparts to future works. Finally, we used X-ray spectral fitting of the fast-spinning and X-ray dim MSP 47 Tuc aa to place tight constraints on  $r$ -mode heating processes.

## 2 OBSERVATIONS AND DATA REDUCTION

We used data from the 2000, 2002, and 2014–2015 *Chandra* ACIS observations of the GC 47 Tuc.<sup>1</sup> While the five 2000 observations (described in Grindlay et al. 2001a) were carried out with the ACIS-I CCD array at telescope focus, the eight 2002 observations (described in H05) and the six 2014–2015 observations (described in Bogdanov et al. 2016) were acquired with the ACIS-S CCD array. All the 2014–2015 observations, as well as short observations in 2000 and 2002, were taken using a subarray, which reduced the

<sup>1</sup> We omitted the 2005–2006 *Chandra* observations of 47 Tuc taken with the HRC-S camera, since these have significantly higher background.

**Table 1.** Summary of *Chandra* observations.

ObsID	Start time	Exposure (ks)	Aim point	CCDs
78	2000-03-16 07:18:30	3.87	ACIS-I	1/4
953	2000-03-16 08:39:44	31.67	ACIS-I	6
954	2000-03-16 18:03:03	0.85	ACIS-I	1/8
955	2000-03-16 18:33:03	31.67	ACIS-I	6
956	2000-03-17 03:56:23	4.69	ACIS-I	1/4
2735	2002-09-29 16:59:00	65.24	ACIS-S	5
3384	2002-09-30 11:38:22	5.31	ACIS-S	1/4
2736	2002-09-30 13:25:32	65.24	ACIS-S	5
3385	2002-10-01 08:13:32	5.31	ACIS-S	1/4
2737	2002-10-02 18:51:10	65.24	ACIS-S	5
3386	2002-10-03 13:38:21	5.54	ACIS-S	1/4
2738	2002-10-11 01:42:59	68.77	ACIS-S	5
3387	2002-10-11 21:23:12	5.73	ACIS-S	1/4
15747	2014-09-09 19:32:57	50.04	ACIS-S	1/8
15748	2014-10-02 06:17:00	16.24	ACIS-S	1/8
16527	2014-09-05 04:38:37	40.88	ACIS-S	1/8
16528	2015-02-02 14:23:34	40.28	ACIS-S	1/8
16529	2014-09-21 07:55:51	24.7	ACIS-S	1/8
17420	2014-09-30 22:56:03	9.13	ACIS-S	1/8

Note. Subarrays are indicated by fractional numbers of CCDs.

frame time, and thus reduced ‘pile-up’—of the (incorrect) recording of two photons that landed on nearby pixels during one frame as a single event. Subarray observations, however, only read out a portion of the CCD, encompassing the core of 47 Tuc. All the observations are summarized in Table 1. The total *Chandra* exposure time of 47 Tuc is 540 ks.

The data were reduced using CIAO version 4.8<sup>2</sup> and CALDB version 4.7.1, in accordance with standard CIAO science threads.<sup>3</sup> All the observations were reprocessed from the original level 2 event files following the default ACIS reprocessing steps. The reprocessing applies the sub-pixel event-repositioning algorithm EDSER<sup>4</sup> (Li et al. 2004), which improves on-axis image resolution, thereby improving the resolution for the crowded centre of 47 Tuc. The intrinsic on-axis point spread function (PSF) of the *Chandra* mirrors for a typical spectrum is reasonably represented by a Gaussian with full width at half-maximum (-FWHM) of 0.4 arcsec (*Chandra* POG,<sup>5</sup> chapter 7). The ACIS detector pixels are 0.492 arcsec in size, so oversampling them is clearly beneficial. The effects of using the EDSER algorithm on the *Chandra* PSF are yet to be calibrated. We limited the energy range to 0.5–6 keV and covered the cluster out to 2.79 arcmin, the half-mass radius used by H05, in each observation. (We use this limiting radius for compatibility with H05 and other *Chandra* studies of GCs, motivated by the dominance of non-cluster sources outside that radius.) We matched the astrometry of all the observations to ObsID 2735. Pile-up at the level of 10–15 per cent (the maximum seen for any source in 47 Tuc) has a very small effect on astrometric corrections, as proven by the lack of detectable differences in alignment with their optical counterparts between the brightest X-ray sources and fainter X-ray sources in 47 Tuc (Edmonds et al. 2003a). We merged all the observations to obtain a deeper event file and subsequently produced images binned to a

quarter of an arcsecond (half a pixel), for source detection. We also created exposure maps and aspect histograms for all the CCDs, for each observation, to use with the ACIS-EXTRACT (AE) package,<sup>6</sup> version 2016feb1, as discussed later.

### 3 ANALYSIS

#### 3.1 Source detection

We employed the two source detection algorithms, CIAO’s *wavdetect*<sup>7</sup> algorithm (Freeman et al. 2002) and the independent *pwdetect*<sup>8</sup> algorithm (Damiani et al. 1997). The *wavdetect* tool employs a Mexican-Hat wavelet-based source detection algorithm that detects probable sources within a data set using significant correlations of source pixels with wavelets of different scales. For this, we created images binned to half a pixel in the 0.5–6, 0.5–2 and 2–6 keV energy bands, using scales of 1.414, 2.0, 2.828, 4, 5.656 and 8.0 pixels, with a source detection significance threshold of  $10^{-6}$ , which should result in one false detection per ACIS chip. We chose to use larger source detection scales in order to permit the detection of point sources farther away from the aimpoint but within the half-mass radius. The half-pixel binning of the images ensured that even in the crowded centre of 47 Tuc, *wavdetect* could separate close sources in spite of the larger source detection scales.

*pwdetect* is also a wavelet-based source detection algorithm, which performs a multiscale analysis of the data, thus allowing the detection of both pointlike and moderately extended sources in the entire field of view. Compared to *wavdetect*, it is more effective in the detection of faint sources close to brighter ones (as seen by Heinke et al. 2003a and Forestell et al. 2014). To use *pwdetect*, we created images binned to one pixel in the aforementioned energy bands, using scales from 0.5 to 1 arcsec, and a final detection threshold of  $5.1\sigma$ , which should also result in one false detection per ACIS chip. We also created a merged event file consisting exclusively of split-pixel events, as this is known (e.g. Zurek et al. 2016) to improve *Chandra*’s angular resolution at the cost of  $\sim 25$  per cent of the total counts. Although, in our case, we lost about  $\sim 33$  per cent of the total counts.

We found an improved performance for *wavdetect* as compared to previous reports (e.g. H05) in separating sources in the crowded cluster centre, which we attribute to the EDSER algorithm and use of the half-pixel binned image. We also corroborated the performance of *pwdetect* in detecting faint sources close to bright ones. Despite the 12 detection runs, an additional seven possible sources near the crowded cluster centre can still be clearly identified by eye. We created a combined source list with all the sources identified from the detection runs and by eye. Subsequent comparison with the source list from H05 leads us to identify 20 additional sources. We add these to our source catalogue as well, and refine our combined source catalogue further using the AE package, detailed by Broos et al. (2010).

Spectra and background were extracted for each source in the catalogue using the AE package (explained in detail in Section 3.2). Subsequently, the positions of these sources were refined by calculating the centroid of the data within a preliminary extraction region. When the probability of the extracted counts being produced by fluctuations in the background (*PROB\_NO\_SOURCE*) was above a

<sup>2</sup> <http://xc.cfa.harvard.edu/ciao/>

<sup>3</sup> <http://xc.harvard.edu/ciao/threads/index.html>

<sup>4</sup> <http://xc.harvard.edu/ciao/why/acissubpix.html>

<sup>5</sup> <http://xc.cfa.harvard.edu/proposer/POG/html/>

<sup>6</sup> [http://www2.astro.psu.edu/xray/docs/TARA/ae\\_users\\_guide.html](http://www2.astro.psu.edu/xray/docs/TARA/ae_users_guide.html)

<sup>7</sup> <http://xc.cfa.harvard.edu/ciao/threads/wavdetect/>

<sup>8</sup> [http://www.astropa.unipa.it/progetti\\_ricerca/PWDetect/](http://www.astropa.unipa.it/progetti_ricerca/PWDetect/)

**Table 2.** 47 Tuc basic X-ray source properties, combined data set.

Name Label	CXOGlb J	Position $\alpha$ (h:m:s)	$\delta$ ( $^{\circ}$ : $'$ : $''$ )	$P_{\text{err}}$ (arcsec)	$f_{\text{PSF}}$	$f_{\text{EXP}}$	Counts		Luminosity 0.5–6 keV ( $10^{30}$ erg s $^{-1}$ )	Notes
							0.5–2 keV	0.5–6 keV		
42	002404.3–720458	00:24:04.251	–72:04:57.976	0.277	0.90	1.00	20 696.0 $^{+205.7}_{-203.6}$	29 194.4 $^{+335.8}_{-331.7}$	1151.6 $^{+13.2}_{-13.1}$	X9
46	002403.5–720452	00:24:03.500	–72:04:51.888	0.276	0.90	1.00	43143.4 $^{+296.4}_{-294.3}$	45417.4 $^{+352.1}_{-294.3}$	1027.9 $^{+8.0}_{-6.7}$	X7
58	002401.0–720453	00:24:00.956	–72:04:53.137	0.278	0.90	1.00	23 852.4 $^{+220.6}_{-218.5}$	25 271.7 $^{+267.3}_{-255.5}$	574.2 $^{+6.1}_{-5.8}$	X5
56	002402.1–720542	00:24:02.125	–72:05:41.982	0.286	0.90	0.98	2428.3 $^{+70.7}_{-68.6}$	3392.6 $^{+115.2}_{-111.1}$	169.5 $^{+5.8}_{-5.6}$	X6
27	002406.4–720443	00:24:06.378	–72:04:42.956	0.284	0.90	1.00	4729.0 $^{+98.5}_{-96.4}$	5555.4 $^{+140.2}_{-136.1}$	167.7 $^{+4.2}_{-4.1}$	X10
47	002403.5–72055	00:24:03.456	–72:05:05.212	0.287	0.90	1.00	2167.9 $^{+66.9}_{-64.8}$	3074.0 $^{+109.6}_{-105.5}$	113.4 $^{+4.0}_{-3.9}$	–
2	002415.9–720436	00:24:15.880	–72:04:36.336	0.289	0.90	0.98	1529.5 $^{+56.0}_{-54.0}$	2250.7 $^{+94.6}_{-90.5}$	96.1 $^{+4.0}_{-3.9}$	X13
1	002417.0–720427	00:24:16.966	–72:04:27.160	0.290	0.90	0.97	1478.9 $^{+55.9}_{-53.9}$	1970.5 $^{+88.1}_{-83.9}$	75.3 $^{+3.4}_{-3.2}$	–
36	002404.9–720455	00:24:04.915	–72:04:55.402	0.295	0.90	1.00	235.1 $^{+26.8}_{-24.3}$	977.5 $^{+67.5}_{-62.8}$	73.0 $^{+5.0}_{-4.7}$	–
30	002406.0–720456	00:24:06.001	–72:04:56.104	0.290	0.90	1.00	1456.7 $^{+55.6}_{-53.5}$	1983.3 $^{+89.0}_{-84.8}$	71.6 $^{+3.2}_{-3.1}$	X19
45	002403.8–720423	00:24:03.759	–72:04:22.912	0.291	0.90	0.87	1302.6 $^{+52.6}_{-50.6}$	1700.8 $^{+81.8}_{-77.7}$	64.0 $^{+3.1}_{-3.0}$	–
64	002357.7–72052	00:23:57.678	–72:05:01.918	0.292	0.90	0.99	964.4 $^{+45.6}_{-43.6}$	1400.9 $^{+76.8}_{-72.7}$	58.1 $^{+3.2}_{-3.0}$	–
51	002402.8–720449	00:24:02.810	–72:04:49.066	0.291	0.90	1.00	1232.8 $^{+52.3}_{-50.1}$	1629.5 $^{+81.8}_{-77.4}$	56.7 $^{+2.8}_{-2.7}$	–
25	002407.1–720546	00:24:07.139	–72:05:45.730	0.294	0.90	0.98	854.5 $^{+43.2}_{-41.1}$	1112.6 $^{+67.2}_{-63.0}$	55.6 $^{+3.4}_{-3.2}$	X11
8	002410.7–720426	00:24:10.747	–72:04:25.644	0.295	0.89	0.96	380.0 $^{+27.7}_{-25.6}$	904.8 $^{+61.6}_{-57.5}$	54.4 $^{+3.7}_{-3.5}$	–
23	002407.8–720441	00:24:07.802	–72:04:41.473	0.292	0.89	1.00	1060.0 $^{+46.9}_{-44.8}$	1376.8 $^{+72.0}_{-67.9}$	43.8 $^{+2.3}_{-2.2}$	–
125	002354.0–720350	00:23:53.985	–72:03:50.069	0.294	0.90	0.82	951.5 $^{+45.3}_{-43.2}$	1038.9 $^{+60.2}_{-55.9}$	43.1 $^{+2.5}_{-2.3}$	X4
15	002408.5–72050	00:24:08.477	–72:05:00.269	0.297	0.90	0.98	330.3 $^{+25.3}_{-23.2}$	711.0 $^{+54.4}_{-50.2}$	39.4 $^{+3.0}_{-2.8}$	–
53	002402.5–720511	00:24:02.533	–72:05:11.202	0.296	0.90	1.00	605.2 $^{+36.6}_{-34.5}$	846.7 $^{+60.2}_{-56.0}$	32.0 $^{+2.3}_{-2.1}$	–
37	002405.0–720451	00:24:04.966	–72:04:51.272	0.292	0.89	1.00	1290.6 $^{+53.5}_{-51.4}$	1360.9 $^{+67.2}_{-59.1}$	31.9 $^{+1.6}_{-1.4}$	–
32	002405.6–720449	00:24:05.647	–72:04:49.159	0.295	0.90	1.00	768.2 $^{+41.6}_{-39.5}$	937.7 $^{+61.7}_{-57.4}$	29.5 $^{+1.9}_{-1.8}$	–
17	002408.3–720431	00:24:08.306	–72:04:31.393	0.294	0.90	0.99	916.0 $^{+44.8}_{-42.7}$	1042.5 $^{+62.1}_{-57.8}$	28.8 $^{+1.7}_{-1.6}$	–
114	002419.4–720335	00:24:19.364	–72:03:34.729	0.301	0.90	0.90	397.0 $^{+30.2}_{-28.2}$	492.2 $^{+45.8}_{-41.5}$	24.5 $^{+2.3}_{-2.1}$	–
29	002406.1–720449	00:24:06.059	–72:04:49.004	0.301	0.90	1.00	357.3 $^{+29.2}_{-27.0}$	495.2 $^{+47.8}_{-43.6}$	19.7 $^{+1.9}_{-1.7}$	MSP-W
117	002413.8–72032	00:24:13.794	–72:03:02.178	0.304	0.90	0.96	293.4 $^{+26.2}_{-24.1}$	372.6 $^{+40.7}_{-36.4}$	18.5 $^{+2.0}_{-1.8}$	–
122	002403.8–720622	00:24:03.847	–72:06:21.586	0.304	0.90	0.99	286.0 $^{+26.0}_{-23.9}$	363.1 $^{+40.1}_{-35.8}$	18.3 $^{+2.0}_{-1.8}$	–
16	002408.3–720436	00:24:08.298	–72:04:35.720	0.302	0.90	0.99	310.2 $^{+26.9}_{-24.8}$	449.9 $^{+45.4}_{-41.2}$	18.1 $^{+1.8}_{-1.7}$	–
120	002411.1–720620	00:24:11.099	–72:06:19.973	0.307	0.90	0.96	214.0 $^{+22.8}_{-20.7}$	287.2 $^{+36.9}_{-32.6}$	17.1 $^{+2.2}_{-1.9}$	–
44	002403.7–720459	00:24:03.694	–72:04:58.980	0.303	0.90	1.00	297.3 $^{+27.4}_{-25.2}$	414.4 $^{+44.7}_{-40.3}$	15.5 $^{+1.7}_{-1.5}$	–
126	002344.8–72062	00:23:44.828	–72:06:01.976	0.312	0.90	0.81	107.7 $^{+15.6}_{-13.4}$	208.8 $^{+31.5}_{-27.1}$	15.5 $^{+2.3}_{-2.0}$	–
24	002407.3–720449	00:24:07.339	–72:04:49.325	0.300	0.89	1.00	463.5 $^{+32.5}_{-30.5}$	532.9 $^{+46.0}_{-41.7}$	14.8 $^{+1.3}_{-1.2}$	–
20	002407.9–720455	00:24:07.938	–72:04:54.736	0.300	0.90	1.00	429.7 $^{+31.0}_{-28.9}$	515.0 $^{+45.2}_{-40.9}$	14.7 $^{+1.3}_{-1.2}$	–

*Notes.* The source positions have been adjusted to place them on to the radio frame, using the X-ray detections of 19 radio MSPs. Positional errors are quoted in arcseconds for both RA and Dec., and are the 95 per cent error circles, as calculated by H05. The PSF fraction ( $f_{\text{PSF}}$ ) and the fractional exposure time ( $f_{\text{EXP}}$ ) have also been mentioned for each source. The Notes column indicates *c* for sources which appear confused, and *m* for sources added manually, and includes other reported names (X for *ROSAT* sources, MSP-\* for MSPs). A portion of this table is shown here for guidance; the full table is available in the electronic edition of the journal.

threshold value of  $\sim 10$  per cent (Weisskopf et al. 2007), the source was removed from the catalogue, followed by a refinement of the positions. This process was repeated till no further pruning of the catalogue was necessary.

This pruning left us with 370 X-ray sources detected within the cluster half-mass radius, as catalogued in Table 2. The source positions are centroid positions, which were further corrected by matching the astrometry with that of the previously known MSPs in 47 Tuc (detailed in Section 3.3). For the positional error of each source, we quote the radius of the 95 per cent error circle ( $P_{\text{err}}$ ), calculated using the empirical formula derived by H05 from applying *wavdetect* on simulated data. Here the source positions were ordered by decreasing luminosity in the 0.5–6 keV band, and have

been labelled accordingly. We retained the W numbering scheme of Grindlay et al. (2001a), as extended in H05 to cover all the sources previously identified from the 2000 and 2002 observations, extending it further to cover the additional ones identified in this work. The W numbers for five sources, which have been resolved into multiple sources, and six sources which were previously identified but were not detected in our analysis, have been omitted. Sources with *PROB\_NO\_SOURCE* greater than  $\sim 1.5$  per cent but less than  $\sim 10$  per cent have been retained in our final catalogue, but since their detection is marginal, they have been marked as *c* in Table 2. The sources identified by eye have been marked as *m*.

Fig. 1 identifies all the sources found within the cluster half-mass radius, while Fig. 2 identifies those within the crowded core,



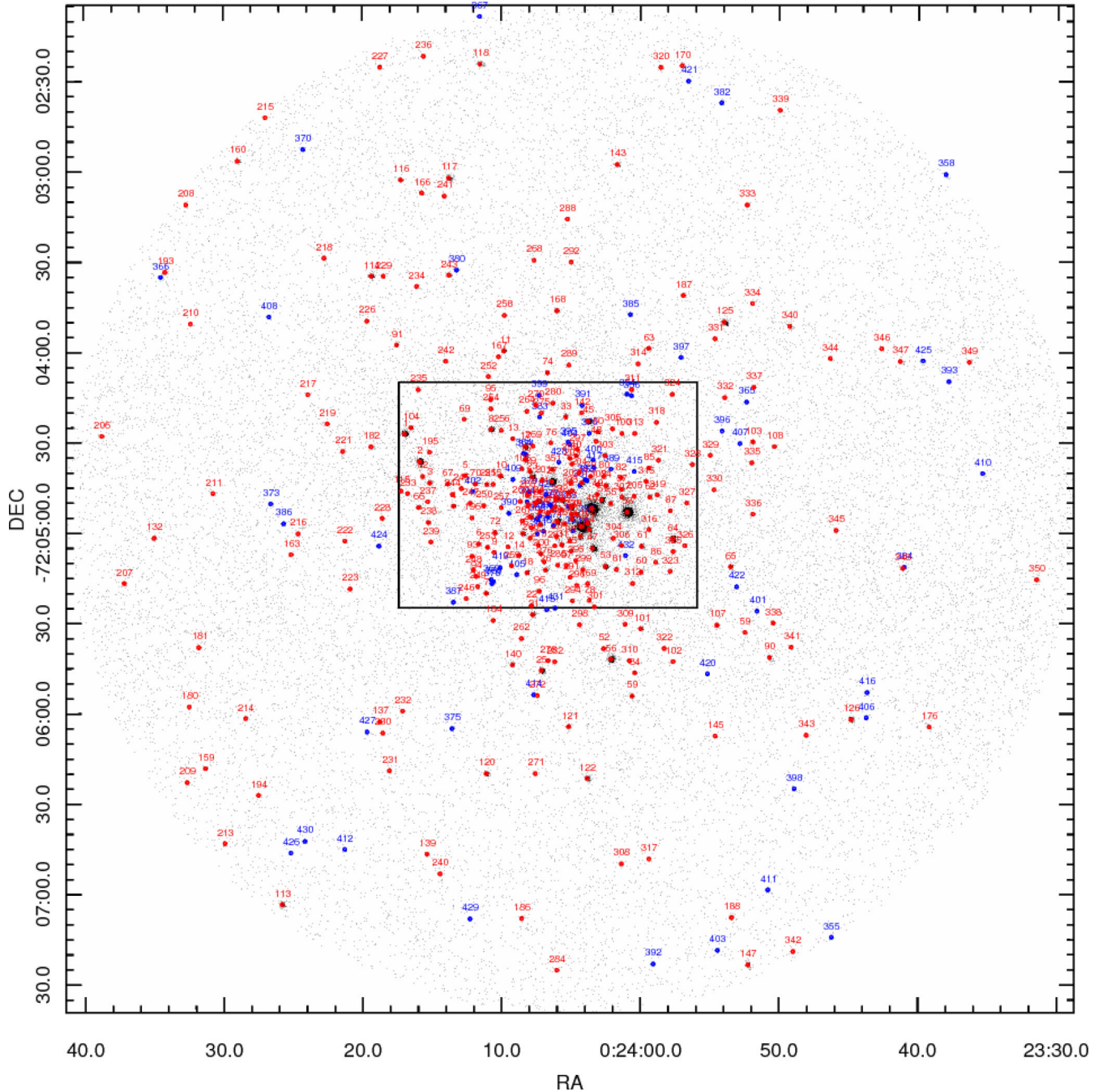


**Figure 1.** Combined 0.5–6 keV image of all *Chandra* ACIS observations of 47 Tuc, binned to half a pixel. The centres of the circles represent the positions, while the labels indicate the W numbers of the X-ray sources. The sources shown in red were already identified by H05, while those in blue have been identified in this work. The sources within the inset box are shown in Fig. 2.

both plotted on an image produced by combining data from the 19 ACIS observations binned to half a pixel in the 0.5–6 keV energy band. The sources shown in red were already identified by H05 while those in blue, numbering 81, have been newly identified in this work. The newly identified sources are either fainter than the previously identified ones, or are located close to bright sources. Fig. 3 shows a merged exposure map (in units of  $\text{cm}^2 \text{s}$ , encoding the telescope effective area and the amount of time each location was imaged) covering the half-mass radius, illustrating that we obtain the highest sensitivity in the core. Fig. 4 shows a representative true-

colour image of the combined data obtained from the 19 merged observations made from the 0.2–1.5, 1.5–2.5 and 2.5–8 keV data.

### 3.2 Extraction and photometry

From the positions defined in our initial source catalogue, source and background spectra were extracted. Events were selected from each observation, for each source, from within a region that encompassed 90 percent of the PSF centred on each catalogue position, or a region of reduced size if the sources were too crowded. The typical on-axis

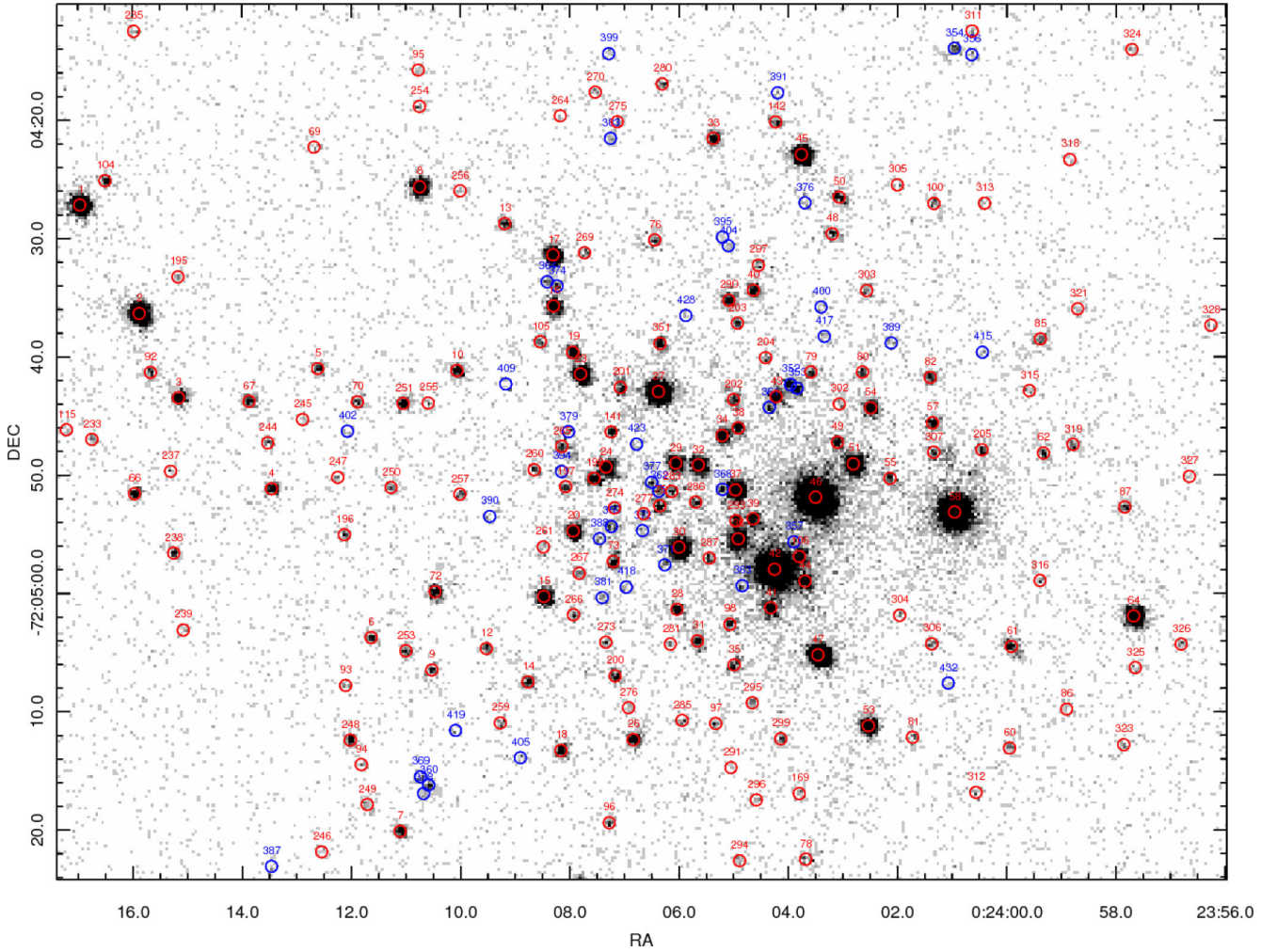


Figure 2. Same as that of Fig. 1 but within the inset box.

extraction radius was  $\sim 0.9$  arcsec. From these events, source and background spectra were extracted by the `ae_standard_extraction` tool, which also generated effective area files and response matrices by calling the appropriate `CIAO` tools. Background extractions included at least 50 counts, involving masks designed to accurately assess the local background due to neighbouring point sources as well as the instrumental background, and sampled pixels from areas outside all source extraction regions (for details, see Broos et al. 2010).

After extracting photons, AE runs the `CHECK_POSITIONS` stage, which can produce estimates of the source position by several methods, including performing image reconstruction on a crowded field with a maximum likelihood method (Broos et al. 2010). We obtained these image reconstruction positions for faint sources that suffered significant crowding in the core region; these objects have been listed in Table 3. The average shift between these positions and the centroid positions quoted in Table 2 for the corresponding sources are 0.34 arcsec in RA and 0.13 arcsec in Dec.

These extractions were repeated until the positions of sources were well determined and no further pruning was needed. Background-subtracted photometry was calculated in several bands. We also determined the number of counts for each catalogue source in the 0.5–2 and 2–6 keV bands, and also photon fluxes (quoted as ‘FLUX2’ in AE; that is, net counts divided by the mean effective

area in the band, and by the exposure time) in the 0.5–1, 1–2, 2–4 and 4–6 keV bands.

We calculated the total luminosity in the 0.5–6 keV band, using `XSPEC` version 12.9.<sup>9</sup> We calculated the conversion from observed photon fluxes to (unabsorbed) energy fluxes using the `XSPEC` `VMEKAL` model, with a typical temperature of 2 keV, and accounting for Galactic absorption with the `TBABS` model (Wilms, Allen & McCray 2000), to the combined spectrum. We chose the `VMEKAL` model since we expect these faint sources to be dominated by chromospherically active binaries and CVs, both of which have X-ray spectra well represented by `MEKAL` models (e.g. H05). Using the known cluster absorbing column, distance and metal abundances, we computed a  $\text{photon cm}^{-2} \text{s}^{-1}$  to  $\text{erg cm}^{-2} \text{s}^{-1}$  conversion for the different flux bands, and subsequently used these conversions to calculate luminosity in the 0.5–6 keV band, for all the sources (as shown in Table 2).

### 3.3 Astrometric corrections

The final refined positions of our sources were further corrected to the known radio-timing positions of 19 out of the 23 MSPs with

<sup>9</sup> <http://heasarc.gsfc.nasa.gov/docs/xanadu/xspec/>



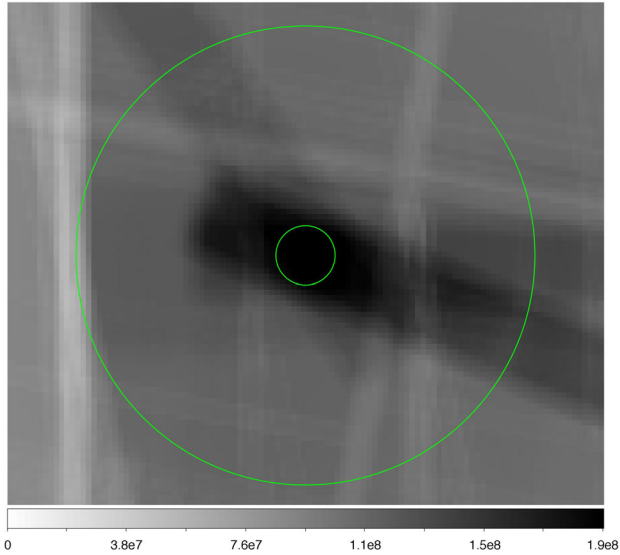


**Figure 3.** Combined exposure map from the 19 merged observations of 47 Tuc in units of  $\text{cm}^2$ . The core (0.36 arcmin) and half-mass (2.79 arcmin, as used by H05) radii are marked for reference. Features in the exposure map include reduced exposure due to a chip gap at the east edge of the half-mass radius from the 2002 observations, chip gaps crossing the interior from the 2000 observations, and regions of increased exposure due to the positions of the 2014–2015 subarray observations (all of which covered the cluster core).

well-constrained positions in 47 Tuc. The known positions for 16 of these MSPs were obtained from Freire et al. (2003) while that for the MSP 47 Tuc ab was obtained from Pan et al. (2016), for 47 Tuc W from Ridolfi et al. (2016), and for 47 Tuc Y from Freire et al. (2017). The astrometric corrections were carried out using CIAO with a matching radius of 1 arcsec.

Disregarding the counterparts of 47 Tuc S and 47 Tuc F for reasons explained in Section 4, and 47 Tuc L, whose counterpart is affected by being too close to a bright source, we have constrained the positions of our sources to a standard deviation of  $\sim 0.16$  arcsec in RA and  $\sim 0.08$  arcsec in Dec., of the other MSPs. The deviations for individual MSPs are listed in Table 4. This table also includes the positions for MSPs 47 Tuc R and Z, whose positions have been reported in Freire et al. (2017), and 47 Tuc aa, whose position will be reported in Freire & Ridolfi (in preparation). Only three of the 22 X-ray counterparts lie farther than the H05 95 per cent error circle from the radio position, suggesting that most of the X-ray counterparts are correct counterparts. Two of the three counterparts that are farther than expected from their radio positions (R and L) lie in the wings (1.5 and 2.6 arcsec distance, respectively) of brighter sources, which is likely to affect their estimated X-ray positions.

We shifted the radio positions of all the MSPs by 5 arcsec in four directions, and searched for X-ray sources within 0.5 arcsec of these shifted positions, thus estimating the probability of chance superposition with unrelated sources. This false match probability per source per trial was found to be 0.0375, indicating that of order one MSP is expected to coincide with another X-ray source within 47 Tuc. This is consistent with the calculation in H05 of a 3.5 per cent chance for any given source above 20 counts to fall within 0.5 arcsec of another such source. Any MSPs where this situation occurs would be detected as the sum of the X-ray emission of the MSP and the other source. H05 speculates that this may explain the detection of X-ray variability from 47 Tuc O, as the X-ray emission from 47 Tuc O is not expected to be variable on these time-scales, while

it would not be surprising, for instance, from a chromospherically active binary.

### 3.4 Optical counterparts

We identified candidate optical counterparts from the lists of variable stars given by A01 for five of the newly identified X-ray sources (Table 5). Astrometric corrections to the *HST* positions of the A01 binaries (0.269 arcsec in RA and 0.085 arcsec in Dec.) were made by aligning *HST* counterparts to the five brightest X-ray sources with identifications by Edmonds et al. (2003a) to their X-ray positions derived in this work. These X-ray sources were found to have a rms offset of  $\sim 0.025$  arcsec in RA and  $\sim 0.035$  arcsec in Dec. with their corresponding astrometrically corrected *HST* positions. We identified variable stars from A01 as candidate optical counterparts to our newly identified X-ray sources within thrice the rms offsets in RA and Dec. from the X-ray positions (0.13 arcsec; Table 5). All the candidate optical counterparts identified in this work, except WF2-V19, were suggested by H05 to be faint and/or confused X-ray sources, which we were able to identify with our deeper X-ray source list.

### 3.5 Radial distribution

In Fig. 5, we plotted the radial distance from the centre of 47 Tuc,  $\alpha = 00^{\text{h}}24^{\text{m}}05^{\text{s}}.29$ ,  $\delta = -72^{\circ}04'52''.3$  (de Marchi et al. 1996), in units of  $\text{arcmin}^2$ , for the 81 sources newly identified by this work. The sources in the core are most likely cluster members, while sources near the outskirts are probably dominated by background extragalactic sources. The distribution of expected background extragalactic objects should be homogeneous over the half-mass radius of 47 Tuc, so following H05, it appears that the sources in the central  $2 \text{ arcmin}^2$  are dominated by cluster members, while those in the remainder of the field are not primarily cluster members. As the remainder of the field contains 26 new sources, we estimated (assuming that new non-cluster members in the central region are added at the same rate) that of order 35 new detections are not cluster members, while roughly 46 new cluster members have been added.

## 4 SPECTRAL ANALYSIS

In this paper, we concentrated only on spectral analysis of the newly identified X-ray counterparts to MSPs. Spectra were obtained for the X-ray counterparts of MSPs 47 Tuc F, S, Z, aa and ab separately for the 2000, 2002 and 2014–2015 observations using AE (2014–2015 observations were not used to fit the X-ray spectra of 47 Tuc aa). Their positions are shown in Fig. 6. For the MSPs 47 Tuc F, Z, and aa, we used the C-statistic, to perform spectral fitting with few photons (Cash 1979), with bins of five counts. On the other hand, the spectra of 47 Tuc S and ab (where we could bin to 10 counts per bin) were fitted using the  $\chi^2$  statistic.

Each was first fitted to an XSPEC power law, PEGPWRLW, then to the XSPEC blackbody model, BBODYRAD, and finally to an NS hydrogen atmosphere model (NSATMOS; Heinke et al. 2006), keeping the hydrogen column density frozen to the cluster value in each case (using the TBABS absorption model with *wilm* abundances; Wilms et al. 2000), as it could not be reasonably constrained by spectral fits. The steep photon indices, over 2.2 ( $3.02^{+0.48}_{-0.46}$ ,  $3.09^{+0.44}_{-0.39}$ ,  $2.89^{+0.28}_{-0.27}$ ,  $2.29^{+0.59}_{-0.55}$  and  $2.92^{+0.43}_{-0.38}$  for 47 Tuc F, S, Z, aa and ab, respectively), obtained for all five MSPs with power-law model fits

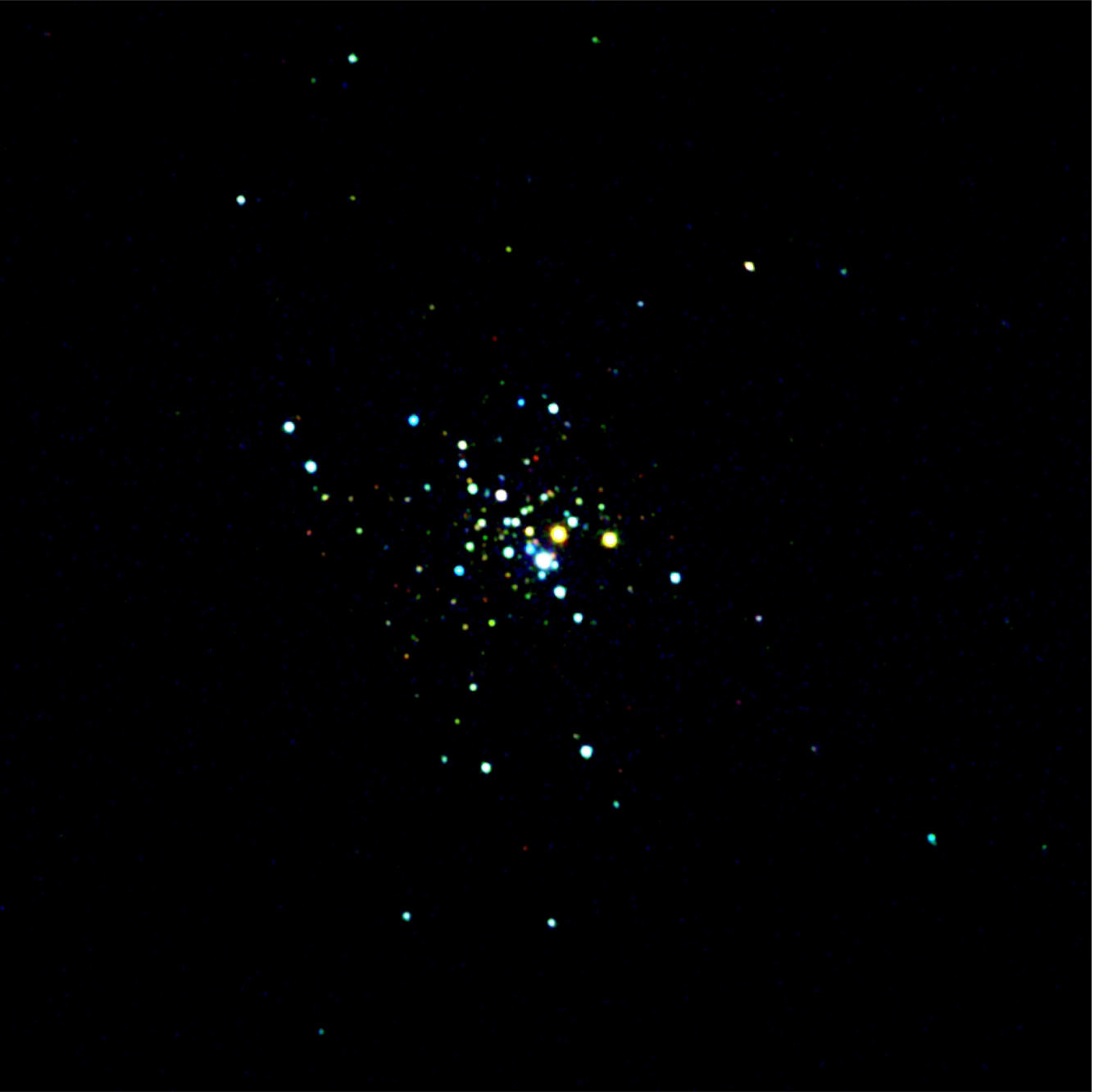


**Figure 4.** True colour image for the 19 merged observations of 47 Tuc within the half-mass radius. It was constructed from a 0.2–1.5 keV image (red), a 1.5–2.5 keV image (green) and a 2.5–8 keV image (blue). All images were binned to 0.25 arcsec pixels, smoothed using ds9 with a Gaussian kernel of radius 3 pixels, and then combined.

implied that the spectra are too steep to be produced by typical pulsar magnetospheres, and are likely dominated by thermal emission from the NS surface. For the NSATMOS model, the NS mass and radius were fixed to  $1.4 M_{\odot}$  and 11 km, respectively, and the distance to 4.53 kpc, while the normalization was left free (physically interpreted as a variable portion of the surface radiating), as used by, for example, Bogdanov et al. (2006).

The results of both model fits for the temperature, radius and luminosity (0.5–6 keV) are given in Table 6. Our fitted temperatures are generally consistent with those found for 47 Tuc MSPs by Bogdanov et al. (2006), who found average black-

body/NSATMOS temperatures of 0.18/0.10 keV (range 0.13–0.24/0.07–0.16 keV). Our fitted radii are also generally consistent (Bogdanov et al. 2006 found average blackbody/NSATMOS radii of 0.17/0.81 km, ranges of 0.08–0.29/0.28–1.75 km), though 47 Tuc aa has the smallest inferred radius and the smallest inferred luminosity, of 47 Tuc MSPs. NSATMOS fits are shown in Figs. 7 and 8. We used the XSPEC command ‘goodness 1000’, which generates 1000 Monte Carlo simulations of the chosen model to see what fraction have a lower fitting statistic than the actual data, to test whether a model is a good fit (e.g. Forestell et al. 2014).



**Table 3.** Alternative positions of crowded sources, obtained from image reconstruction.

Label	$\alpha$ (h:m:s)	$\delta$ (°:':")
24	00:24:07.342	−72:04:49.303
41	00:24:04.321	−72:05:01.280
43	00:24:04.218	−72:04:43.403
44	00:24:03.687	−72:04:58.948
75	00:24:06.331	−72:04:52.626
106	00:24:03.786	−72:04:56.870
198	00:24:07.577	−72:04:50.308
265	00:24:08.176	−72:04:47.834
283	00:24:06.141	−72:04:51.384
293	00:24:04.955	−72:04:53.839
348	00:23:41.132	−72:05:11.252
352	00:24:03.972	−72:04:42.323
353	00:24:03.836	−72:04:42.708
357	00:24:03.947	−72:04:55.776
360	00:24:10.578	−72:05:16.260
361	00:24:04.344	−72:04:44.360
362	00:24:06.373	−72:04:51.384
363	00:24:04.880	−72:04:59.552
364	00:24:08.409	−72:04:33.704
368	00:24:05.239	−72:04:51.280
369	00:24:10.718	−72:05:15.608
371	00:24:06.240	−72:04:57.428
374	00:24:08.246	−72:04:34.104
377	00:24:06.507	−72:04:50.675
378	00:24:10.687	−72:05:17.117
379	00:24:08.003	−72:04:46.268
384	00:23:40.935	−72:05:11.242
404	00:24:05.081	−72:04:30.677

#### 4.1 Msp 47 Tuc aa

47 Tuc aa was discovered by Pan et al. (2016), and its timing solution will be presented in Freire & Ridolfi (in preparation). We identified W96 as its X-ray counterpart. The possibility of W96 being an MSP was previously suggested by Edmonds et al. (2003b), based on the lack of an optical counterpart, and H05 based on its X-ray properties. It is one of the fainter detected sources, with only 33.5 counts. We did not use the 2014–2015 observations to fit the X-ray spectra of 47 Tuc aa, since they lay on the edge of the ACIS subarray. The fit is relatively poor (the fraction of simulated spectra with a worse C statistic than the data is only 5.7 per cent), apparently due to excess emission at high energies (see Fig. 6), but adding a power-law component (with spectral index between 1 and 2) does not improve the fit. The fitted BBODYRAD temperature of  $0.20^{+0.06}_{-0.02}$  keV is consistent with other MSPs in 47 Tuc (Bogdanov et al. 2006), but the inferred effective radius of  $0.07^{+0.06}_{-0.07}$  or  $0.20^{+0.53}_{-0.20}$  km (for blackbody or NSATMOS fits, respectively) is the smallest in 47 Tuc. Between 0.5–6 keV, it has a luminosity of  $0.7^{+0.3}_{-0.2} \times 10^{30}$  ergs s<sup>−1</sup> (for a blackbody fit, or  $0.9^{+0.7}_{-0.8} \times 10^{30}$  erg s<sup>−1</sup> for the NSATMOS model), making it also the faintest MSP yet identified in 47 Tuc.

We also performed fits to 47 Tuc aa assuming emission from the entire surface, in order to calculate constraints on r-mode heating of the interior. In these fits, we used the model TBABS\*(NSATMOS+NSATMOS), where one of the NSATMOS models used a fixed normalization of 1 (corresponding to emission from the entire surface) while the normalization of the other was allowed free (corresponding to emission from the poles). For these

**Table 4.** Deviations in X-ray positions of individual MSPs from their known radio positions.

Label	MSP	$\Delta\alpha$ (arcsec)	$\Delta\delta$ (arcsec)	X-ray err (arcsec)	$\Delta/X_{\text{err}}$
7	E	−0.22	−0.02	0.32	0.69
11	U	−0.06	−0.06	0.33	0.26
13	N	−0.04	−0.07	0.33	0.24
19	G,I	0.05, 0.2	−0.02, −0.04	0.31	<0.21
28	Z	−0.01	−0.10	0.32	0.31
29	W	0.01	−0.09	0.30	0.30
39	O	0.12	0.00	0.31	0.39
63	J	0.12	−0.02	0.32	0.38
67	D	−0.08	−0.08	0.32	0.35
74	H	0.08	0.10	0.33	0.40
82	Y	0.00	−0.08	0.33	0.24
96	aa	0.02	−0.12	0.36	0.34
104	Q	0.34	−0.04	0.33	1.04
105	T	−0.01	−0.16	0.34	0.47
106	L	0.63	0.03	0.31	2.03
107	M	0.08	−0.14	0.34	0.47
108	C	0.27	−0.12	0.35	0.84
198	R	−0.44	−0.11	0.32	1.42
265	ab	−0.32	−0.03	0.33	0.97
352	S	−0.25	0.03	0.32	0.79
353	F	−0.27	−0.15	0.34	0.64

*Note.* – The columns give the *wavdetect* number, MSP radio detection name (e.g. 47 Tuc E), deviations in RA and Dec., the 95 per cent confidence error circle radius on the X-ray position (following H05), and the total deviation divided by the X-ray error.

**Table 5.** New optical counterpart identifications.

W	A01 Name	$\Delta\alpha$ (arcsec)	$\Delta\delta$ (arcsec)	Type	Period (d)
363	PC1-V28	−0.036	0.089	BY Dra	1.16
368	PC1-V07	−0.012	−0.027	W UMa S.Det.	0.4188
399	WF2-V19	−0.038	0.057	BY Dra	1.56
414	WF4-V09	0.005	0.063	BY Dra	1.37
424	WF3-V21	−0.036	−0.049	BY Dra	4.03

*Note.* – Separations ( $\Delta\alpha$  and  $\Delta\delta$ ) are defined as *Chandra* minus *HST* positions. Types and periods are from A01.

fits only, we explored several NS radii; 11, 12 and 12.5 km. Larger stars have weaker constraints on the total luminosity, so we focus on the 12.5 km radius case, selected as roughly the top end of the range of the most plausible NS radius estimates (see e.g. Lattimer & Steiner 2014). The 90 per cent confidence limit on the (unredshifted) surface temperature is  $2.80 \times 10^5$ ,  $2.68 \times 10^5$  and  $2.62 \times 10^5$  K for 11, 12 or 12.5 km, respectively, leading to (bolometric, calculated as 0.01–10 keV) unredshifted luminosity limits of  $3.27 \times 10^{30}$  erg s<sup>−1</sup>,  $3.43 \times 10^{30}$  erg s<sup>−1</sup> or  $3.50 \times 10^{30}$  erg s<sup>−1</sup>, respectively.

#### 4.2 Msp 47 Tuc ab

47 Tuc ab was recently discovered by Pan et al. (2016), who published its timing solution, this was recently updated by Freire et al. (2017). We identify W265 as its X-ray counterpart, although, as noted by H05, W265 appears to consist of multiple confused sources. W265 is well fitted by blackbody or NSATMOS models with inferred temperature and radius consistent with other MSPs in 47 Tuc, suggesting that the observed X-ray emission at this location is indeed mostly due to 47 Tuc ab. Its 0.5–6 keV (blackbody

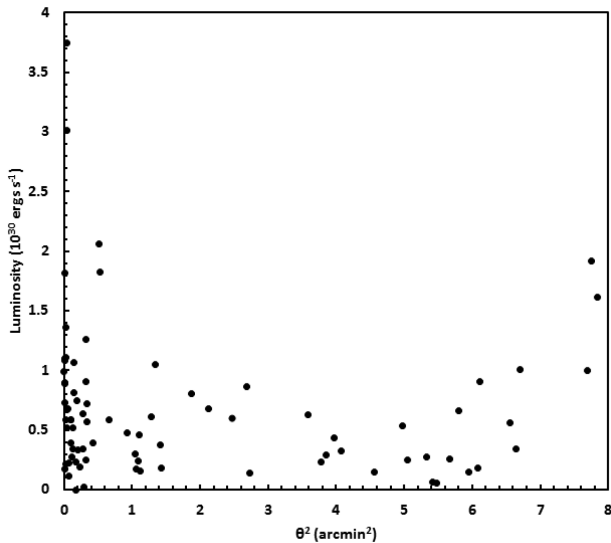


**Figure 5.** Distribution of luminosity versus radial distance from the centre of 47 Tuc, plotted in units of  $\text{arcmin}^2$ , for sources identified by this work. Outside  $\theta^2 = 2 \text{ arcmin}^2$ , the flat distribution suggests a uniform spatial distribution.

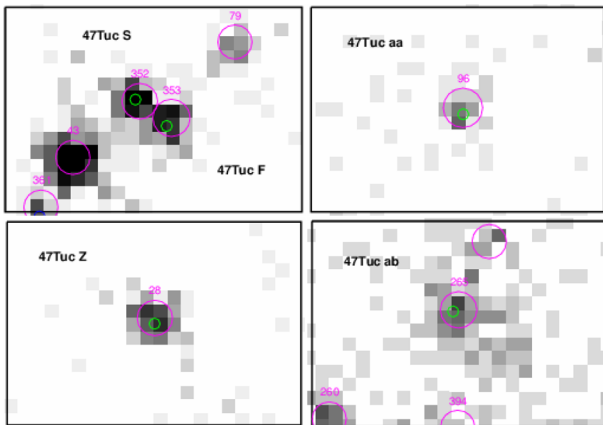


**Figure 6.** The radio-identified spatial positions of the MSPs studied in this work are shown in green. Their identified X-ray counterparts are indicated in magenta. The background image is a combined 0.5–6 keV image of all *Chandra* ACIS observations of 47 Tuc, binned to half a pixel.

fit) luminosity of  $1.6^{+0.3}_{-0.4} \times 10^{30} \text{ ergs s}^{-1}$  makes it the second-most X-ray faint MSP identified in 47 Tuc, after 47 Tuc aa.

### 4.3 Msp 47 Tuc Z

Freire et al. (2017) have found a timing solution for MSP 47 Tuc Z. We identify W28 as its X-ray counterpart. Edmonds et al. (2003b) and H05 both previously suggested that W28 was a possible MSP. The spectral fit to blackbody or NSATMOS models is good, and the inferred parameters are typical of MSPs in 47 Tuc.

### 4.4 Msp 47 Tuc S

X-ray emission from MSPs 47 Tuc S and 47 Tuc F was previously studied together, as they had not been resolved (Bogdanov et al. 2006). With the increased resolution in this work; however, we were able to analyse them separately, identifying W352

as the X-ray counterpart of MSP S. The positional discrepancy, 0.25 arcsec in RA and 0.03 arcsec in Dec. from its known radio position, is slightly larger than typical, which is likely due to crowding. The spectral fits to blackbody or NSATMOS models are good, and the inferred parameters are typical of MSPs in 47 Tuc.

### 4.5 Msp 47 Tuc F

We identify W353 as the X-ray counterpart to 47 Tuc F, at 0.27 arcsec in RA and 0.15 arcsec in Dec. from its known radio position. As for 47 Tuc S, the positional discrepancy is larger than average, which we attribute to crowding in this region. The spectral fits to blackbody or NSATMOS models are acceptable, and the inferred parameters are typical of 47 Tuc MSPs. We note that the temperatures for 47 Tuc F and 47 Tuc S individually are consistent with the average temperature for the merged source quoted by Bogdanov et al. (2006).

## 5 DISCUSSION

### 5.1 Source catalogue

By merging all observations taken with the ACIS instrument of the *Chandra* X-ray Observatory, using the EDSEER algorithm, and overbinned the final image, we were able to obtain significantly higher resolution. This, in conjunction with detection algorithms like *wavdetect* and *pwddetect*, and algorithms and tools from AE, allowed us to identify 81 new sources in 47 Tuc, over half of which are present in and near the crowded core region. We thus find a total of 370 sources within the half-mass radius of 47 Tuc. While the newly detected sources in the outskirts of 47 Tuc are probably dominated by background extragalactic sources (considering their relatively uniform spatial distribution), those near the crowded core are likely to be a mixture of ABs and CVs in the cluster, almost certainly dominated by ABs (see the luminosity functions in fig. 13 of H05). There may also be a few MSPs and quiescent LMXBs, although new MSPs are likely to be among sources that are newly resolved (e.g. 47 Tuc F and S), rather than sources at the detection limit, based on the known X-ray luminosity function of GC MSPs (see H05). MSPs generally have luminosities (0.5–2.5 keV) in the range  $10^{30}$ – $10^{31} \text{ erg s}^{-1}$ , while quiescent LMXBs range from  $\sim 10^{31}$ – $10^{33} \text{ erg s}^{-1}$ . H05 was already complete for uncrowded sources with luminosities above  $8 \times 10^{29} \text{ ergs s}^{-1}$  and this work only pushes the detection limit marginally. So the increased sources, we detect are largely due to improvement in the angular resolution and detection efficiency.

The luminosities for these sources, computed from the photometry as explained in Section 3.2, do not always match those obtained by H05 as illustrated in Fig. 9. Sources with higher counts in the 2–6 keV range, notably W42 (X9), seem to show an increased luminosity in this work, whereas sources with lesser counts in this hard band, notably W46 (X7), seem to show a decreased luminosity (though spectral fitting shows that W46/X7 has demonstrated that it is not actually variable; Bogdanov et al. 2016). A likely explanation is the reduced sensitivity of the ACIS-S detector in the lower energy bands, which combined with a single assumed spectral model can produce such apparent variations. (For example, the expected 0.5–6 keV count rate for an on-axis source described by a power law with photon index 1.8 and the cluster  $N_H$  decreases by 28 per cent from the 2002 to 2014 ACIS-S observations; for a 2 keV VMEKAL model, the decrease is 30 per cent.) It is to be noted

**Table 6.** X-ray spectral properties of MSPs.

MSP	Model	$kT$ (keV)	$R_{\text{eff}}$ (km)	$L_X$ (0.5–6 keV) ( $10^{30}$ ergs s $^{-1}$ )	Goodness (percent)	Statistic ( $C/\chi^2$ )	Dof
aa	BBODYRAD	$0.20^{+0.06}_{-0.02}$	$0.07^{+0.06}_{-0.07}$	$0.7^{+0.3}_{-0.2}$	2.88	11.91	9
	NSATMOS	$0.14^{+0.09}_{-0.06}$	$0.20^{+0.53}_{-0.20}$	$0.9^{+0.7}_{-0.8}$	5.71	10.45	9
ab	BBODYRAD	$0.21^{+0.05}_{-0.04}$	$0.09^{+0.07}_{-0.03}$	$1.6^{+0.3}_{-0.4}$	(10.1)	14.65	9
	NSATMOS	$0.11^{+0.04}_{-0.03}$	$0.45^{+0.58}_{-0.45}$	$1.5^{+4.8}_{-1.2}$	(18.2)	12.58	9
Z	BBODYRAD	$0.20^{+0.02}_{-0.02}$	$0.14^{+0.03}_{-0.03}$	$2.8^{+0.4}_{-0.4}$	18.27	29.69	25
	NSATMOS	$0.11^{+0.02}_{-0.02}$	$0.68^{+0.38}_{-0.22}$	$2.6^{+3.1}_{-1.6}$	18.48	24.61	25
S	BBODYRAD	$0.18^{+0.02}_{-0.02}$	$0.20^{+0.06}_{-0.06}$	$3.1^{+0.5}_{-0.5}$	(9.3)	14.92	11
	NSATMOS	$0.09^{+0.02}_{-0.02}$	$1.12^{+0.74}_{-0.47}$	$2.8^{+5.4}_{-1.8}$	(10.7)	14.45	11
F	BBODYRAD	$0.19^{+0.04}_{-0.03}$	$0.14^{+0.06}_{-0.05}$	$1.8^{+0.8}_{-0.3}$	7.57	15.27	12
	NSATMOS	$0.10^{+0.03}_{-0.03}$	$0.75^{+0.75}_{-0.75}$	$2.1^{+6.0}_{-1.6}$	8.10	12.76	12

*Note.* – The BBODYRAD and NSATMOS models used CFLUX and the FLUX command, respectively, to determine the unabsorbed luminosity. MSPs ab & S were fitted with the  $\chi^2$  statistic (and the null hypothesis probability is quoted rather than the C-stat ‘goodness’ statistic), the rest were fitted with the C-statistic.

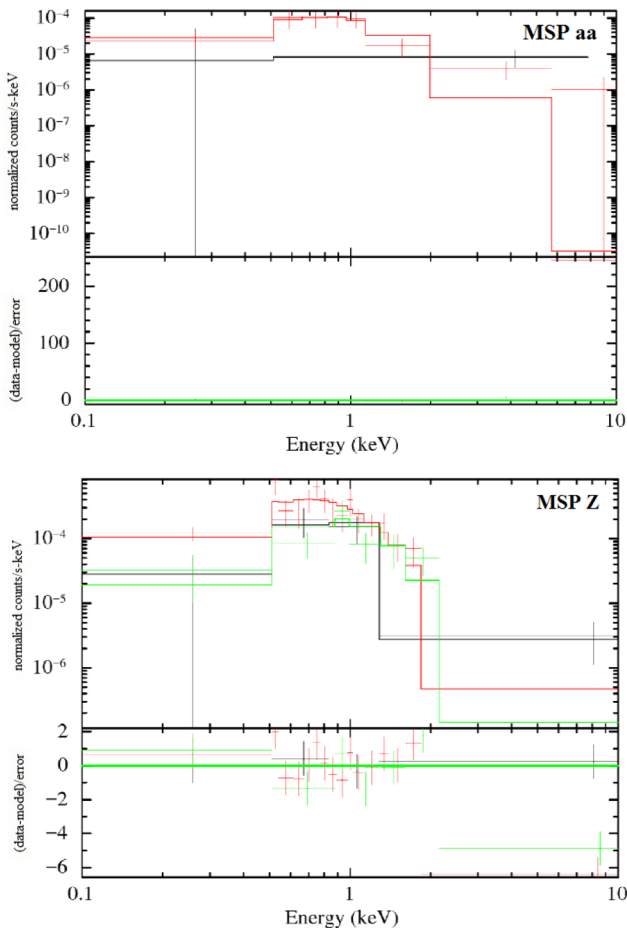


**Figure 7.** NSATMOS spectral fits to the X-ray counterparts of MSPs 47 Tuc aa and 47 Tuc Z. The spectra were modelled with an absorbed NS hydrogen atmosphere (top panels are data and model, lower panels are residuals). The data and spectral fit are shown in black, red and green for the 2000, 2002 and 2014–2015 observations, respectively, all of which were fit simultaneously.

that the individual luminosities of these sources must be obtained more accurately by fitting different spectral models suitable for different objects. W42 (X9) has been comprehensively studied by Bahramian et al. (2017), who confirm this source as an ultracompact

X-ray binary with a C/O white dwarf donor and a possible black hole primary.

## 5.2 Msp polar caps

From the spectral fits for the recently discovered MSPs 47 Tuc aa, 47 Tuc ab and 47 Tuc Z, and freshly resolved MSPs 47 Tuc S and 47 Tuc F, we obtained their temperatures and luminosities, which were found to be consistent with those of most other MSPs in 47 Tuc, analysed by Bogdanov et al. (2006). In comparison to the BBODYRAD model, the NSATMOS hydrogen atmosphere model gives lower estimates of the temperatures (Table 2), while the unabsorbed luminosity estimates from the two models are consistent. Since the NS surface is almost certainly covered with a hydrogen atmosphere in these MSPs (Zavlin & Pavlov 1998; Bogdanov et al. 2007), the (larger) NSATMOS model estimates of the emitting radii are more realistic. As discussed by Bogdanov et al. (2006), these estimates of the emitting radius will vary from the true polar cap sizes, as high-quality spectra of the nearby MSP PSR J0437–4715 show that at least two, probably three, thermal components are required (Zavlin et al. 2002; Bogdanov 2013; Guillot et al. 2016), likely from different parts of the polar caps.

It has long been predicted that the size of the polar cap region of a radio pulsar,  $R_{\text{pc}} = (2\pi R_{\text{NS}}/(cP))^{1/2} R_{\text{NS}}$  (e.g. Lyne & Graham-Smith 2012), where  $R_{\text{NS}}$  is the radius of the NS having period  $P$ , depends inversely on the spin period. It thus follows that MSPs in 47 Tuc, having shorter periods, on average, than those in NGC 6752, should have larger polar caps (given similar luminosities). By fitting the effective radii measurements of MSPs in 47 Tuc, NGC 6752 and NGC 6397, with a power law in spin period, Forestell et al. (2014) found a best-fitting index of  $-0.65 \pm 0.40$  ( $1\sigma$  error bars), consistent with the predicted index of  $-0.5$ . We plotted the spin periods against the inferred MSP effective radii (from BBODYRAD) for all the MSPs in 47 Tuc, NGC 6752 and NGC 6397, adding six new pulsars to 47 Tuc (those studied here, and 47 Tuc X from Ridolfi et al. 2016; Fig. 10). Fitting the effective radii measurements with a power law in spin period, we found a best-fitting index of  $-0.41 \pm 0.27$  ( $1\sigma$  error bars). This slightly increases the evidence for a correlation by reducing the  $1\sigma$  uncertainty, and is still consistent with the theoretically predicted index of  $-0.5$ . Dispersion into this correlation is expected from the (unknown) differences



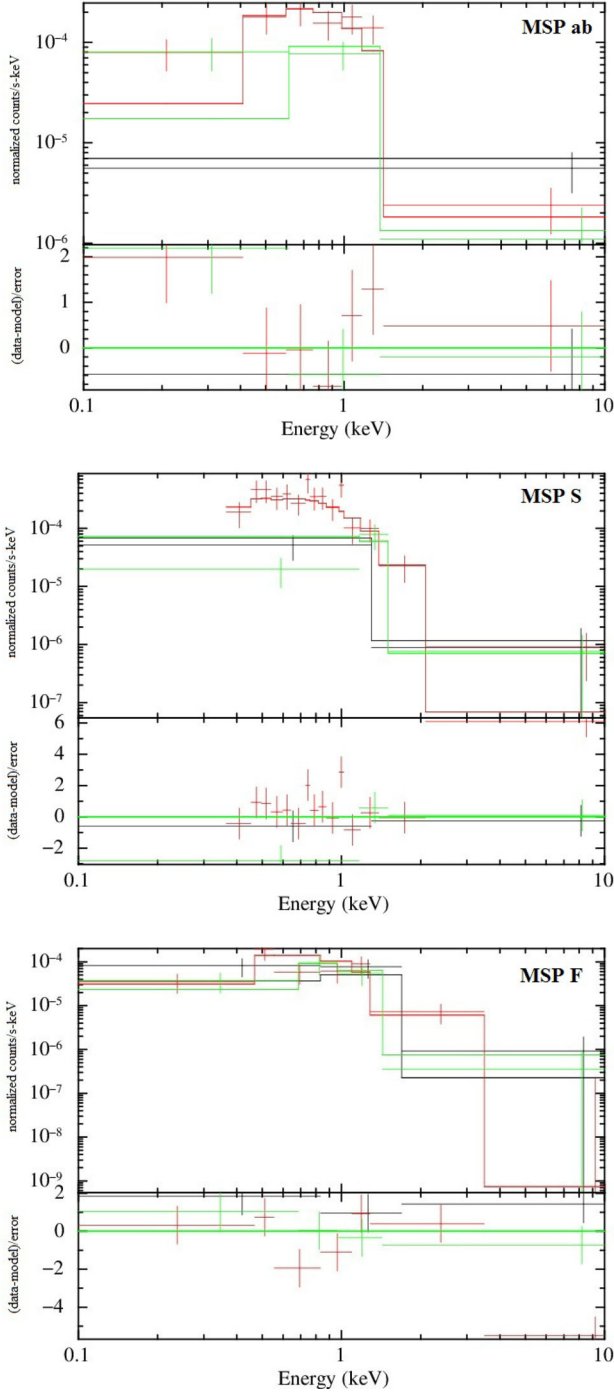


Figure 8. Same as Fig. 7 but for 47 Tuc ab, 47 Tuc S and 47 Tuc F.

in geometries of the pulsars, and by variations in the strength of unmodelled non-thermal radiation.

## 6 UPPER LIMIT FOR SURFACE TEMPERATURE OF MSP 47 TUC AA AND CONSTRAINTS ON R MODES

An intriguing consequence of the low X-ray luminosity of 47 Tuc aa is the constraint it allows us to impose upon internal heating in rapidly spinning NSs. MSPs should be in thermal balance, because their thermal evolution time-scale is much shorter than their

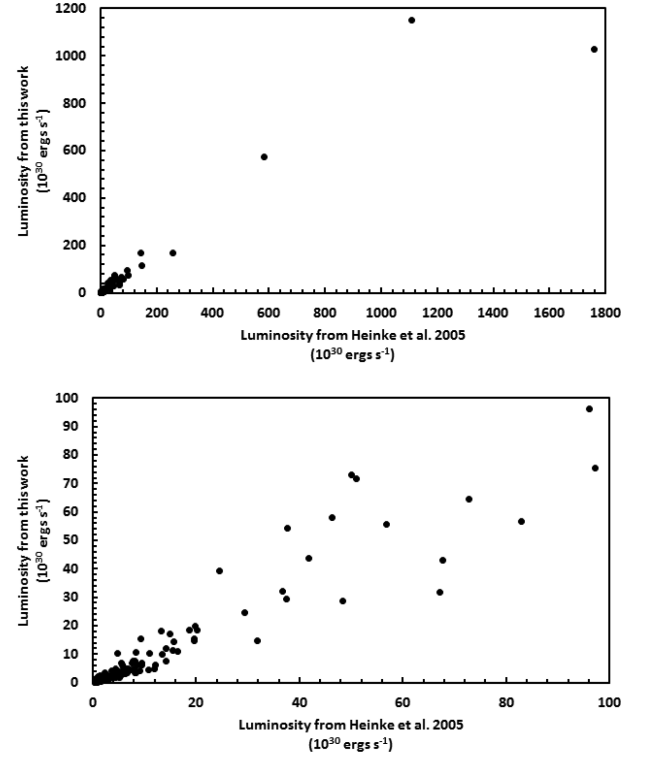


Figure 9. Comparison of luminosities in the 0.5–6 keV band derived by this work with that obtained by H05. The top panel shows all the sources identified in both works, while the bottom panel shows those sources with luminosities less than  $100 \times 10^{30} \text{ ergs s}^{-1}$ .

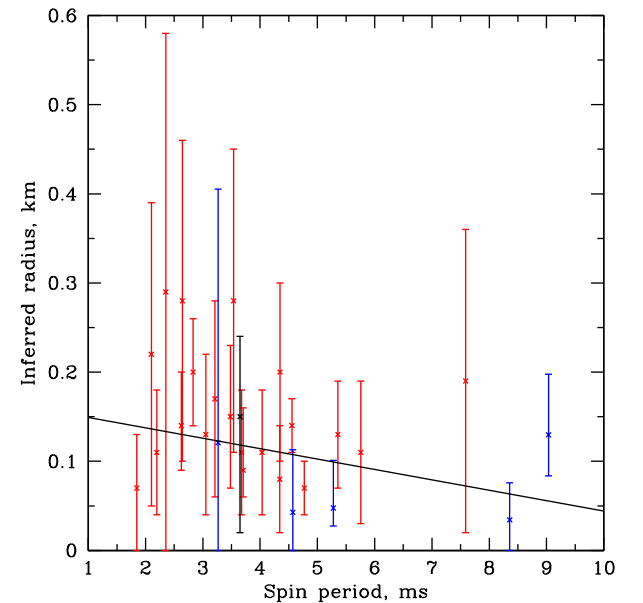


Figure 10. Fitted (BBODYRAD) polar cap radius against spin period for MSPs in 47 Tuc (red), NGC 6397 (black) and NGC 6752 (blue). The best-fitting power law is indicated, with a best-fitting slope  $-0.41 \pm 0.27$ , consistent with the predicted index of  $-0.5$ .

spin-down time-scale. Thus the total heating power should be compensated by cooling, which depends on the MSP temperature.

The surface temperature of 47 Tuc aa is low enough (see Section 4.1) to exclude strong neutrino emission from the bulk of the star (see e.g. Chugunov et al. 2017 for more detailed discussion). Thus, the total cooling power of this source can be estimated almost directly from observations: it equals the thermal emission from the entire surface, excluding hot spots (i.e. from the component with a fixed normalization of 1 in Section 4.1),<sup>10</sup>

$$L_{\text{cool}} \approx L \leq 3.5 \times 10^{30} \text{ erg s}^{-1}, \quad (1)$$

providing the same constraint to the total heating power, which can be presented as a sum of internal heating mechanisms (namely, superfluid vortex creep Alpar et al. 1984, rotochemical heating Reisenegger 1995, rotation-induced deep crustal heating Gusakov et al. 2015), and possible heating produced by the dissipation of unstable oscillation modes (e.g. r modes, Andersson et al. 2002; Reisenegger & Bonačić 2003b; Chugunov et al. 2017; Schwenzer et al. 2017).

We start from the internal heating. Its power  $Q$  is generally proportional to the (intrinsic) spin-down rate (Gonzalez & Reisenegger 2010; Gusakov et al. 2015), which can be bounded as  $\dot{\nu} \geq -5 \times 10^{-15} \text{ s}^{-2}$  on the basis of the accurate timing solution (Freire & Ridolfi, in preparation) and accounting for the strongest possible negative acceleration in the cluster gravitational field (Freire et al. 2017). The typical spin-down power of other MSPs with X-ray luminosity  $\sim 10^{30} \text{ erg s}^{-1}$  (see, e.g. fig. 8 in Forestell et al. 2014) suggests that real spin-down rate of 47 Tuc aa is slower, but for estimates below we apply robust bound from the radio observations. Following Chugunov et al. (2017), to estimate the internal heating power we appeal to the rotation-induced deep crustal heating (Gusakov et al. 2015), which is associated with the same physics as deep crustal heating in accreting NSs (Brown, Bildsten & Rutledge 1998). Namely, compression of the accreted material (due to subsequent accretion for accreting NSs, or due to spin-down in case of MSPs) leads to nuclear reactions in the crust and production of heat. This mechanism does not depend on the uncertain parameters of superfluid transition in the star and thus it is rather robust. For the parameters of 47 Tuc aa it gives

$$Q \gtrsim Q_{\text{DCH}} \approx 1.8 \times 10^{30} \frac{\text{erg}}{\text{s}} \left( \frac{R}{12.5 \text{ km}} \right)^7 \left( \frac{M}{1.4 M_{\odot}} \right)^{-2} \times \frac{\nu}{542 \text{ Hz}} \frac{|\dot{\nu}|}{5 \times 10^{-15} \text{ s}^{-2}} \sum_i \frac{P_i}{10^{31} \text{ erg cm}^{-3}} \frac{q_i}{\text{MeV}}, \quad (2)$$

where equation (7) from Gusakov et al. (2015) was applied (parameter  $a$  taken to be  $a = 0.5$ ). Here  $|\dot{\nu}| = -\dot{\nu}$  is absolute value of the intrinsic spin-down rate;  $i$  enumerates the different reactions in the crust;  $P_i$  and  $q_i$  are the threshold pressure and energy production for each reaction, respectively. For all models of the accreted crust discussed by Haensel & Zdunik (2008)  $\sum_i P_i q_i$  lies in the range  $(0.9\text{--}1.5) \times 10^{31} \text{ erg MeV cm}^{-3}$ , making  $Q_{\text{DCH}}$  well constrained, and close to the observational upper bound (1). Note,  $Q_{\text{DCH}}$  is strongly increasing with increase of  $R$  ( $Q_{\text{DCH}} \propto R^7$ ), thus for larger radius or if other internal heating mechanisms are competitive with  $Q_{\text{DCH}}$ , the total heating power can exceed constraint (1) for  $\dot{\nu} = -5 \times 10^{-15} \text{ s}^{-2}$ , suggesting thus that the intrinsic spin-down rate of MSP 47 Tuc aa should be lower. However, we leave

detailed analysis of such constraints beyond the scope of the paper because they are model dependent.

The heating by unstable modes can take place in rapidly rotating NSs due to the Chandrasekhar–Friedman–Schutz (CFS; Chandrasekhar 1970; Friedman & Schutz 1978a,b; Andersson 1998; Friedman & Morsink 1998) instability, driven by emission of gravitational waves. In the absence of dissipation, the CFS instability takes place at an arbitrary rotation rate and results in the exponential growth of a certain class of oscillation modes. The most unstable among them are r modes (predominantly toroidal modes, which are similar to Rossby waves and controlled by the Coriolis force). Dissipation suppresses the instability only up to a threshold spin frequency (which depends on the internal NS temperature; see Fig. 11 and e.g. Haskell 2015 for a recent review). The standard model of r-mode instability (suggested by Lindblom, Owen & Morsink 1998; Owen et al. 1998, see also Gusakov, Chugunov & Kantor 2014a for discussion of recent microphysical updates) assumes a hadronic composition of the NS core and dissipation by shear and bulk viscosity. It stabilizes the NS in the grey region in Fig. 11(a), the unstable (white) region is referred to as the ‘instability window’.

As shown by Ho, Andersson & Haskell (2011) and Haskell, Degenaar & Ho (2012), the observations of transiently accreting NSs (their spin frequencies and internal temperatures are shown in Fig. 11 by dots with error bars associated with uncertainty in thermal insulating envelope composition; data are taken from Gusakov, Chugunov & Kantor 2014b, Chugunov et al. 2017) reveal the inadequacy of the standard model: additional dissipation of r-modes is required to stabilize many observed NSs [i.e. all NSs in the white region of 11(a)]. Chugunov et al. (2017) analyse the formation of MSPs via the recycling scenario (Bisnovatyi-Kogan & Komberg 1976; Alpar et al. 1982; Bhattacharya & van den Heuvel 1991; Papitto et al. 2013) and suggest ‘minimal’ constraints to the instability windows, which allow them to explain the observations of transiently accreting NSs, and the formation of high-frequency MSPs, simultaneously. The corresponding ‘minimally constrained’ instability window is shown in Fig. 11(b). As indicated by Chugunov et al. (2017), strong upper bounds on thermal emission from the entire surface of rapidly rotating MSPs can lead to even stronger constraints, and here we apply the upper limit (1) to this aim.

The first constraint comes from the thermal equilibrium in the current state of the MSP. As discussed by Chugunov et al. (2017), Schwenzer et al. (2017) and Mahmoodifar & Strohmayer (2017), the upper limit for the MSP surface temperature gives an upper bound to the heating by r-modes, and thus to the r-mode amplitude. Substituting the upper limit on the surface temperature from Section 4.1 into equation (12) from Chugunov et al. (2017), we get the constraint

$$\alpha \lesssim 2.5 \times 10^{-9} \quad (3)$$

for the r-mode amplitude (defined as in Lindblom et al. 1998) in MSP 47 Tuc aa. The numerical value corresponds to a radius  $R = 11 \text{ km}$ , which gives the least constraining bound (assuming  $R = 12 \text{ km}$ , we come to  $\alpha \lesssim 2 \times 10^{-9}$ ). It is worthwhile to note that equation (3) is the strongest constraint available for MSPs (Chugunov et al. 2017; Mahmoodifar & Strohmayer 2017; Schwenzer et al. 2017)<sup>11</sup> and accreting NSs (Mahmoodifar &

<sup>10</sup> Here, we use the least constraining limit on the bolometric luminosity from the entire surface of 47 Tuc aa from Section 4.1,  $L \leq 3.50 \times 10^{30} \text{ erg s}^{-1}$  for an assumed radius of 12.5 km.

<sup>11</sup> Schwenzer et al. (2017) suggest a comparable constraint for PSR J1023+0038 ( $\nu = 592.4 \text{ Hz}$ ), but in this paper the surface temperature of PSR

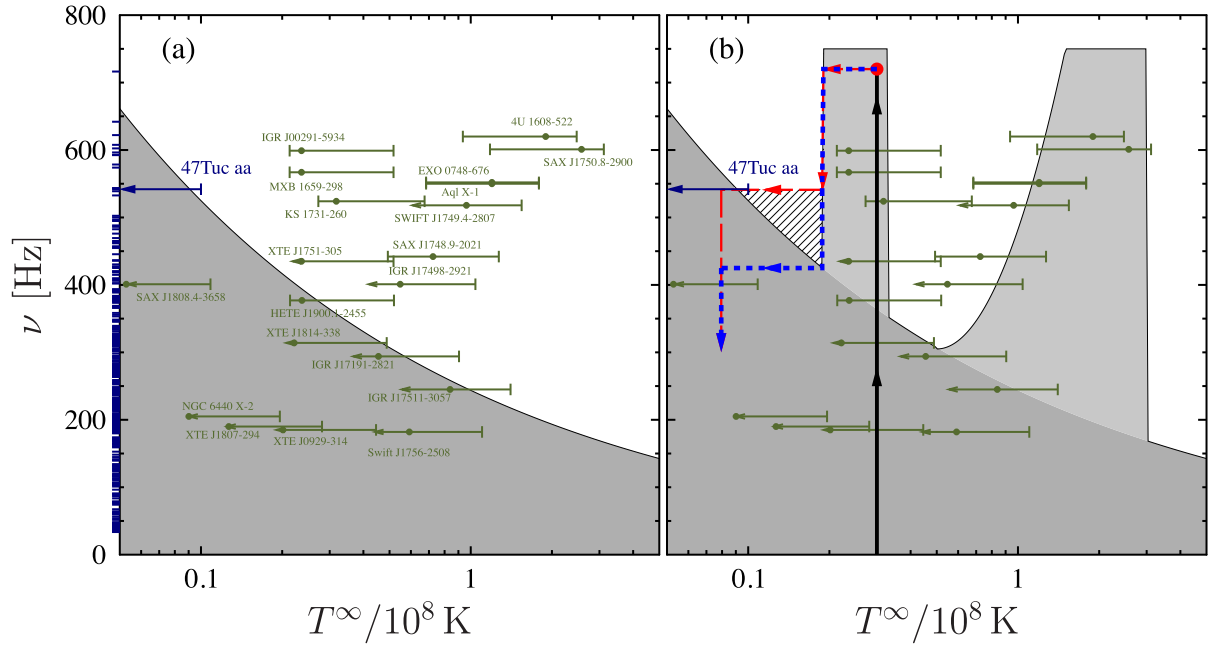


**Figure 11.** Examples of r-mode instability windows in the standard model [panel (a)] and the minimally constrained model [panel (b), see the text for details]. The stability region is shaded in grey; in the white region the r mode is unstable. Temperatures and frequencies of NSs observed in LMXBs are shown by filled circles, while error bars show uncertainties due to the unknown NS envelope composition. The upper limit for the internal temperature of MSP 47 Tuc aa is also marked. Ticks on the left-hand side of  $\nu$  axis show measured MSP frequencies.

Strohmayer 2013). As long as non-linear saturation of the r-mode instability predicted by state-of-art models (Arras et al. 2003; Bondarescu, Teukolsky & Wasserman 2007; Bondarescu & Wasserman 2013; Haskell, Glampedakis & Andersson 2014) takes place at much larger amplitudes, the most natural explanation of the bound (3) is that MSP 47 Tuc aa is stable (at least with respect to CFS instability of r modes). Indeed, the upper limit for the surface temperature of MSP 47 Tuc aa allows us to constrain the redshifted internal temperature as  $T^\infty \leq 10^7$  K even for the iron thermally insulating envelope model by Potekhin, Chabrier & Yakovlev 1997 [a layer of light (accreted) elements with mass  $\Delta M > 10^{-13} M_\odot$  reduce this constraint to  $T^\infty \leq 5 \times 10^6$  K], which is almost enough to guarantee stability of 47 Tuc aa in the standard r-mode instability model [see Fig. 11, panel (a)].

The second constraint, developed by Chugunov et al. (2017), appeals not only to the current state of this MSP, but also to its formation. Namely, it comes from the requirement that the r-mode instability does not prevent cooling of the MSP to the observed temperature, after the end of accretion (and spinup) during the LMXB stage. Chugunov et al. (2017) apply  $T^\infty \lesssim 2 \times 10^7$  K as a fiducial upper limit for internal temperatures of MSPs and demonstrate that it leads to a ‘minimally’ constrained instability window [see Fig. 11(b)]. Since MSP 47 Tuc aa has a lower internal temperature, it puts a stronger constraint on the shape of the instability window.

For the minimally constrained instability window from Chugunov et al. (2017), the evolution of the MSP progenitor during the LMXB stage is unaffected by the r-mode instability, and the evolution-

ary trajectory is shown schematically by the thick solid line in Fig. 11(b). After the end of accretion, the newly born MSP loses accretion-induced heating, cools down and evolves along the low-temperature boundary of the stability peak, where r-modes force spin-down of the MSP and keep it heated (dotted [blue] line in the plot). It is easy to see that this line cannot explain the temperature and spin of MSP 47 Tuc aa (namely, this path predicts its internal temperature to be  $\sim 2 \times 10^7$  K, corresponding to  $T_{\text{eff}}^\infty \sim 6 \times 10^5$  K (an accreted thermal insulating envelope is assumed), which is well above the upper limit obtained in Section 4.1). To allow MSP 47 Tuc aa to cool down enough to be in agreement with observations, the r-mode instability should be suppressed at  $(1-2) \times 10^7$  K at least for the frequency of this pulsar ( $\nu \sim 542$  Hz, Pan et al. 2016). Assuming that there are no isolated regions of r-mode instability, r modes must be stable in the shaded region in Fig. 11(b). In this case, the evolution of MSPs can follow the dashed (red) line in this figure, which is in agreement with observations of MSP 47 Tuc aa.

## 7 CONCLUSIONS

We combined 180 ks of new *Chandra* ACIS data on 47 Tuc with 370 ks of archival data, and used improved algorithms to generate a new source catalogue, finding 81 new sources for a total of 370 within the half-mass region. Roughly half of the new sources are likely associated with the cluster, and half are background active galactic nucleus. We resolved the X-ray emission from MSPs 47 Tuc F and 47 Tuc S, and use recent pulsar timing solutions to identify X-ray emission from the MSPs 47 Tuc aa, 47 Tuc ab and 47 Tuc Z. In general, their X-ray emission is consistent with that of other MSPs in 47 Tuc, though 47 Tuc aa is the X-ray faintest MSP yet measured in 47 Tuc. Comparing the fitted blackbody radii of millisecond pulsar polar caps with their spin rates, we find modest evidence for the expected anticorrelation. Finally, we use our upper limit on the temperature of the surface of the fast-spinning (542 Hz)

J1023+0038 was taken to be  $T_{\text{eff}}^\infty \lesssim 3 \times 10^5$  K (see pulsar at  $\nu = 592$  Hz in Fig. 1 of that paper), without detailed spectral fitting. However, such a strong upper limit is not justified for J1023+0038 (e.g. the joint fit of X-ray spectra by Bogdanov et al. 2011 suggest a higher surface temperature  $T_{\text{eff}}^\infty \sim 4 \times 10^5$  K, leading thus to weaker constraints on the r-mode amplitude).



MSP 47 Tuc aa to constrain the heating of this NS by r modes. We find a constraint on the amplitude of r modes in 47 Tuc aa of  $\lesssim 2.5 \times 10^{-9}$ , the most constraining yet for MSPs. We also use the temperature and rotation frequency of 47 Tuc aa to place a constraint on the shape of the r-mode instability window in NSs.

## ACKNOWLEDGEMENTS

S. Bhattacharya acknowledges support from MITACS for sponsoring his stay at the University of Alberta. COH acknowledges support from an NSERC Discovery Grant and an NSERC Discovery Accelerator Supplement. AR and PCCF gratefully acknowledge financial support by the European Research Council for the ERC Starting grant BEACON under contract no. 279702. AR is a member of the International Max Planck research school for Astronomy and Astrophysics at the Universities of Bonn and Cologne and acknowledges partial support through the Bonn-Cologne Graduate School of Physics and Astronomy. This work was funded in part by NASA Chandra grant GO4-15029A awarded through Columbia University and issued by the Chandra X-ray Observatory Center (CXC), which is operated by the Smithsonian Astrophysical Observatory for and on behalf of NASA under contract NAS803060. This research has made use of the NASA Astrophysics Data System (ADS) and software provided by the CXC in the application package CIAO. *pwddetect* has been developed by scientists at the Osservatorio Astronomico di Palermo G. S. Vaiana, thanks to Italian CNAO and MURST(COFIN) grants.

## REFERENCES

- Albrow M. D., Gilliland R. L., Brown T. M., Edmonds P. D., Guhathakurta P., Sarajedini A., 2001, *ApJ*, 559, 1060 (A01)
- Alpar M. A., Cheng A. F., Ruderman M. A., Shaham J., 1982, *Nature*, 300, 728
- Alpar M. A., Pines D., Anderson P. W., Shaham J., 1984, *ApJ*, 276, 325
- Andersson N., 1998, *ApJ*, 502, 708
- Andersson N., Jones D. I., Kokkotas K. D., 2002, *MNRAS*, 337, 1224
- Arras P., Flanagan E. E., Morsink S. M., Schenk A. K., Teukolsky S. A., Wasserman I., 2003, *ApJ*, 591, 1129
- Bahramian A. et al., 2017, *MNRAS*, 467, 2199
- Bailyn C. D., Grindlay J. E., Garcia M. R., 1990, *ApJ*, 357, L35
- Bassa C. G., Pooley D., Verbunt F., Homer L., Anderson S. F., Lewin W. H. G., 2008, *A&A*, 488, 921
- Becker W., Trümper J., 1999, *A&A*, 341, 803
- Beloborodov A. M., 2002, *ApJ*, 566, L85
- Bhattacharya D., van den Heuvel E. P. J., 1991, *Phys. Rep.*, 203, 1
- Bisnovatyi-Kogan G. S., Komberg B. V., 1976, *Sov. Astron. Lett.*, 2, 130
- Bogdanov S., 2013, *ApJ*, 762, 96
- Bogdanov S., Grindlay J. E., 2009, *ApJ*, 703, 1557
- Bogdanov S., Grindlay J. E., van den Berg M., 2005, *ApJ*, 630, 1029
- Bogdanov S., Grindlay J. E., Heinke C. O., Camilo F., Freire P. C. C., Becker W., 2006, *ApJ*, 646, 1104
- Bogdanov S., Rybicki G. B., Grindlay J. E., 2007, *ApJ*, 670, 668
- Bogdanov S., Archibald A. M., Hessels J. W. T., Kaspi V. M., Lorimer D., McLaughlin M. A., Ransom S. M., Stairs I. H., 2011, *ApJ*, 742, 97
- Bogdanov S., Heinke C. O., Özel F., Güver T., 2016, *ApJ*, 831, 184
- Bondarescu R., Wasserman I., 2013, *ApJ*, 778, 9
- Bondarescu R., Teukolsky S. A., Wasserman I., 2007, *Phys. Rev. D*, 76, 064019
- Broos P. S., Townsley L. K., Feigelson Eric D., Getman K. V., Bauer F. E., Garmire G. P., 2010, *ApJ*, 714, 1582
- Brown E. F., Bildsten L., Rutledge R. E., 1998, *ApJ*, 504, L95
- Cadelano M., Pallanca C., Ferraro F. R., Salaris M., Dalessandro E., Lanzoni B., Freire P. C. C., 2015, *ApJ*, 812, 63
- Camilo F. et al., 2000, *ApJ*, 535, 975
- Cash W., 1979, *ApJ*, 228, 939
- Chandrasekhar S., 1970, *Phys. Rev. Lett.*, 24, 611
- Chugunov A. I., Gusakov M. E., Kantor E. M., 2017, *MNRAS*, 468, 291
- Clark G. W., 1975, *ApJ*, 199, L143
- Cohn H. N. et al., 2010, *ApJ*, 722, 20
- Cool A. M., Haggard D., Arias T., Brochmann M., Dorfman J., Gafford A., White V., Anderson J., 2013, *ApJ*, 763, 126
- Damiani F., Maggio A., Micela G., Sciortino S., 1997, *MNRAS*, 483, 370
- de Marchi G., Paresce F., Stratta M. G., Gilliland R. L., Bohlin R. C., 1996, *ApJ*, 468, L51
- Dempsey R. C., Linsky J. L., Fleming T. A., Schmitt J. H. M. M., 1993, *ApJS*, 86, 599
- Dempsey R. C. et al., 1997, *ApJ*, 478, 358
- Edmonds P. D., Gilliland R. L., Camilo F., Heinke C. O., Grindlay J. E., 2001, *ApJ*, 557, L57
- Edmonds P. D., Gilliland R. L., Camilo F., Heinke C. O., Grindlay J. E., 2002a, *ApJ*, 579, 741
- Edmonds P. D. et al., 2002b, *ApJ*, 564, L17
- Edmonds P. D., Gilliland R. L., Heinke C. O., Grindlay J. E., 2003a, *ApJ*, 596, 1177
- Edmonds P. D., Gilliland R. L., Heinke C. O., Grindlay J. E., 2003b, *ApJ*, 596, 1197
- Forestell L. M., Heinke C. O., Cohn H. N., Lugger P. M., Sivakoff G. R., Bogdanov S., Cool A. M., Anderson J., 2014, *MNRAS*, 441, 757
- Freeman P. E. et al., 2002, *ApJS*, 138, 185
- Freire P. C., Camilo F., Lorimer D. R., Lyne A. G., Manchester R. N., D'Amico N., 2001b, *MNRAS*, 326, 901
- Freire P. C. et al., 2003, *MNRAS*, 320, 1359
- Freire P. C. et al., 2017, *MNRAS*, 471, 857
- Friedman J. L., Morsink S. M., 1998, *ApJ*, 502, 714
- Friedman J. L., Schutz B. F., 1978a, *ApJ*, 221, 937
- Friedman J. L., Schutz B. F., 1978b, *ApJ*, 222, 281
- Gentile P. A. et al., 2014, *ApJ*, 783, 69
- Gilliland R. L. et al., 2000, *ApJ*, 545, L47
- Gonzalez D., Reisenegger A., 2010, *A&A*, 522, A16
- Grindlay J. E., Heinke C. O., Edmonds P. D., Murray S. S., Cool A. M., 2001b, *ApJ*, 563, L53
- Grindlay J. E., Heinke C. O., Edmonds P. D., Murray S. S., 2001a, *Science*, 292, 2290
- Guillot S. et al., 2016, *MNRAS*, 463, 2612
- Gusakov M. E., Chugunov A. I., Kantor E. M., 2014a, *Phys. Rev. D*, 90, 063001
- Gusakov M. E., Chugunov A. I., Kantor E. M., 2014b, *Phys. Rev. Lett.*, 112, 151101
- Gusakov M. E., Kantor E. M., Reisenegger A., 2015, *MNRAS*, 453, L36
- Haensel P., Zdunik J. L., 2008, *A&A*, 480, 459
- Hansen B. M. S. et al., 2013, *Nature*, 500, 51
- Harding A. K., Muslimov A. G., 2002, *ApJ*, 568, 862
- Harris W. E., 1996, *AJ*, 112, 1487
- Haskell B., 2015, *Int. J. Mod. Phys. E*, 24, 1541007
- Haskell B., Degenar N., Ho W. C. G., 2012, *MNRAS*, 424, 93
- Haskell B., Glampedakis K., Andersson N., 2014, *MNRAS*, 441, 1662
- Heinke C. O., Grindlay J. E., Edmonds P. D., Lloyd D. A., Murray S. S., Cohn H. N., Lugger P. M., 2003, *ApJ*, 598, 516
- Heinke C. O. et al., 2010, in Kologera V., van der Sluis M., eds, *AIP Conf. Proc.* 1314, International Conference on Binaries. New York, p. 135
- Heinke C. O., Grindlay J. E., Edmonds P. D., Cohn H. N., Lugger P. M., Camilo F., Bogdanov S., Freire P. C., 2005, *ApJ*, 625, 796 (H05)
- Heinke C. O., Rybicki G. B., Narayan R., Grindlay J. E., 2006, *ApJ*, 644, 1090
- Ho W. C. G., Andersson N., Haskell B., 2011, *Phys. Rev. Lett.*, 107, 101101
- Hong J., van den Berg M., Schlegel E. M., Grindlay J. E., Koenig X., Laycock S., Zhao P., 2005, *ApJ*, 635, 907
- Ivanova N., Heinke C. O., Rasio F. A., Taam R. E., Belczynski K., Fregeau J., 2006, *MNRAS*, 372, 1043
- Ivanova N., Heinke C. O., Rasio F. A., Belczynski K., Fregeau J. M., 2008, *MNRAS*, 386, 553

- Johnston H. M., Kulkarni S. R., Phinney E. S., 1992, in Van Den Heuvel E. P. J., Rappaport S. A., eds, *X-Ray Binaries and the Formation of Binary and Millisecond Radio Pulsars*. Kluwer, Dordrecht, p. 349
- Kargaltsev O., Durant M., Pavlov G. G., Garmire G., 2012, *ApJS*, 201, 37
- Knigge C. et al., 2006, *ApJ*, 641, 281
- Kong A. K. H. et al., 2006, *ApJ*, 647, 1065
- Lattimer J. M., Steiner A. W., 2014, *ApJ*, 784, 123
- Li C. O., Kastner Joel H., Prigozhin G. Y., Schulz N. S., Feigelson E. D., Getman K. V., 2004, *ApJ*, 610, 1204
- Lindblom L., Owen B. J., Morsink S. M., 1998, *Phys. Rev. Lett.*, 80, 4843
- Lu T. N., Kong A. K. H., Verbunt Frank., Lewin W. H. G., Anderson S. F., Pooley D., 2011, *ApJ*, 736, 158
- Lyne A., Graham-Smith F., 2012, *Pulsar Astronomy*, 3rd edn. Cambridge Univ. Press, Cambridge
- Mahmoodifar S., Strohmayer T., 2013, *ApJ*, 773, 140
- Mahmoodifar S., Strohmayer T., 2017, *ApJ*, 840, 94
- Manchester R. N., Lyne A. G., Johnston S., D’Amico N., Lim J., Kniffen D. A., 1990, *Nature*, 345, 598
- Manchester R. N., Lyne A. G., Robinson C., Bailes M., D’Amico N., 1991, *Nature*, 352, 219
- Owen B. J., Lindblom L., Cutler C., Schutz B. F., Vecchio A., Andersson N., 1998, *Phys. Rev. D*, 58, 084020
- Pan Z., Hobbs G., Li D., Ridolfi A., Wang P., Freire P., 2016, *MNRAS*, 459, L26
- Papitto A. et al., 2013, *Nature*, 501, 517
- Paresce F., de Marchi G., 1994, *ApJ*, 427, L33
- Paresce F., de Marchi G., Ferraro F. R., 1992, *Nature*, 360, 46
- Pechenick K. R., Ftaclas C., Cohen J. M., 1983, *ApJ*, 274, 846
- Pooley D. et al., 2002b, *ApJ*, 569, 405
- Pooley D. et al., 2003, *ApJ*, 591, L131
- Potekhin A. Y., Chabrier G., Yakovlev D. G., 1997, *A&A*, 323, 415
- Pryor C., Meylan G., 1993, in Djorgovski S. G., Meylan G., ed., *ASP Conf. Ser. Vol. 50, Structure and Dynamics of Globular Clusters*. Astron. Soc. Pac., San Francisco, p. 357
- Reisenegger A., 1995, *ApJ*, 442, 749
- Reisenegger A., Bonačić A., 2003b, *Phys. Rev. Lett.*, 91, 201103
- Ridolfi A. et al., 2016, *MNRAS*, 462, 2918
- Rivera-Sandoval L. E. et al., 2015, *MNRAS*, 453, 2707
- Rivera-Sandoval L. E. et al., 2017, preprint ([arXiv:1705.07100](https://arxiv.org/abs/1705.07100))
- Roberts M. S. E., McLaughlin M. A., Gentile P. A., Ray P. S., Ransom S. M., Hessels J. W. T., 2015, preprint ([arXiv:1502.07208](https://arxiv.org/abs/1502.07208))
- Robinson C., Lyne A. G., Manchester R. N., Bailes M., D’Amico N., Johnston S., 1995, *MNRAS*, 274, 547
- Schwenzer K., Boztepe T., Güver T., Vurgun E., 2017, *MNRAS*, 466, 2560
- Shara M. M., Bergeron L. E., Gilliland R. L., Saha A., Petro L., 1996, *ApJ*, 471, 804
- Stappers B. W., Gaensler B. M., Kaspi V. M., van der Klis M., Lewin W. H. G., 2003, *Science*, 299, 1372
- Verbunt F., Hut P., 1987, in Helfand D. J., Huang J.-H., eds, *Proc. IAU Symp. 125, The Origin and Evolution of Neutron Stars*. Dordrecht, Reidel, p. 187
- Verbunt F., Lewin W. H. G., 2004, in Lewin W. H. G., van der Klis M., ed., *Compact Stellar X-Ray Sources*. Cambridge Univ. Press, Cambridge
- Verbunt F., Meylan G., 1988, *A&A*, 203, 297
- Weisskopf M. C. et al., 2007, *ApJ*, 644, 1090
- Wilms J., Allen A., McCray R., 2000, *ApJ*, 542, 914
- Zavlin V. E., 2007, *Ap&SS*, 308, 297
- Zavlin V. E., Pavlov G. G., 1998, *A&A*, 329, 583
- Zavlin V. E., Pavlov G. G., Sanwal D., Manchester R. N., Trümper J., Halpern J. P., Becker W., 2002, *ApJ*, 569, 894
- Zurek D. R., Knigge C., Maccarone T. J., Pooley D., Dieball A., Long K. S., Shara M., Sarajedini A., 2016, *MNRAS*, 460, 3660

## SUPPORTING INFORMATION

Supplementary data are available at [MNRAS](https://www.mnras.org/) online.

**Table 2:** 47 Tuc basic X-ray source properties, combined data set.

Please note: Oxford University Press is not responsible for the content or functionality of any supporting materials supplied by the authors. Any queries (other than missing material) should be directed to the corresponding author for the article.

This paper has been typeset from a  $\text{\LaTeX}$  file prepared by the author.